



國立臺灣大學理學院地理環境資源學系

學士班學生論文

Department of Geography

College of Science

National Taiwan University

Bachelor Degree Thesis

台灣西南部造山帶前緣活動構造及地殼變形特性

Active tectonics around an ongoing rapid
surface deformation area in southern Taiwan

許毓芳

Yu-Fang Hsu

指導教授：莊昀叡 博士

Advisor: Ray Y. Chuang, Ph.D.

中華民國 107 年 4 月

April 2018

國立臺灣大學學士班學生論文
口試委員會審定書

台灣西南部造山帶前緣活動構造及地殼變形特性

Active tectonics around an ongoing rapid
surface deformation area in southern Taiwan

本論文係許毓芳君 (b03208018) 在國立臺灣大學地理學系完成之學士班學生論文，於民國 107 年 4 月 25 日承下列考試委員審查通過及口試及格，特此證明

口試委員(3位)：

莊明毅

(簽名)

(指導教授)

黃信樺

黃錦川

系主任：

吳廷宏

(簽名)

(是否須簽章依各院系規定)

謝辭

寫完論文，坐在電腦前，有股莫名的情緒湧上。這篇論文的完成，得之於人者太多，出之於己者太少。需要感謝的人太多了。可我不想只是謝天。因此，我在此依照時間歷程的排序，感謝這些一路走來幫助、啟發我的人們。

感謝我的爸媽當初欣然接受我選擇地理系而沒有打斷我的腿。回顧大學這四年，過得很充實、滿足，也完成許多期望中的事。當我在做人生重大選擇時謝謝你們願意相信正值中二年紀的我。選擇地理系後的人生雖然偶爾會羨慕其他熱門科系的出路，但總得來說我很滿意自己的選擇。謝謝你們讓我做你們的孩子。此外，也感謝我的弟弟。謝謝你願意包容、陪伴我這個不盡責的姐姐。

感謝朱傲祖老師和林俊全老師，因為上你們的課，讓我決定往地質的方向探索。

感謝我的老闆莊昀叡，謝謝你帶來自由的研究風氣，讓我可以做自己喜歡的題目，也感謝你願意提供機會讓我去國外研討會增廣見聞。

感謝中研院的黃信樺老師，這篇學士論文受到你的幫助實在太多。多虧有你我才能完成如此精彩的論文。若沒有你的幫助，就不會投稿日後的英文期刊，大專生計畫結案報告也難以順利完成。在研究上你著實教會我許多事情和精神，我在做這份研究的過程當中也感受到了顯著的成長。

感謝冠芙學姊、孟涵老師，多虧有你們的大力相助，我們才能完成這份文章並投稿出去。

感謝芹姐、均、鈞、昭邑、小叡叡、原瑄、瑜珊、以及大三暑假去中研院地球所暑期實習遇到的所有人。多虧你們，在中研院的那段時光，我都很期待去上班的每一天。謝謝你們很有誠意的回覆我的各種垃圾話。

感謝婉姿、亞嫻、啟見、向捷、依婕、佳穎、Chelsey 等超炫 303 固定班底，我真的很喜歡在研究室不事生產，狂講幹話的時光。謝謝你們的陪伴，我才能在放鬆氣氛下完成各種事情，包括這篇論文。

感謝猥薇、欣儒、承軒、彎彎等各位準研究牲們，或為相同的 deadline 崩潰、或討論未來規劃、或分享研究歷程的種種，這些事都讓我覺得我不孤單。

感謝 205 室友們、Coco、章鈞、莊惟歆、秉宸，以及所有的幹話好夥伴們，我真的很需要幹話調劑身心。跟你們聊天總是可以讓我找回正能量。

感謝可愛的直屬學妹宜芷多次煮食餵飽我，並聽我不斷的垃圾話，以及殷切地讓對我的祈禱參差地翳入了天聽，要是這篇論文得了傅斯年獎我們就去怒吃一發下午茶。

感謝爛軟猴，謝謝你願意包容我這位疑似情緒調節障礙者。有好幾次都是因為你的開導我才能撐過這些難關。

感謝玉山東峰高抬貴手，沒讓我葬身幽谷，我才能活著回來完成論文。



摘要

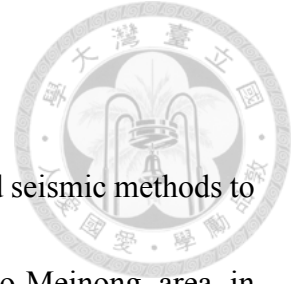
本研究透過 2016 年美濃地震於測地學、地形學及地震學上的分析來探討台灣西南部造山帶前緣的活動構造及地殼變形特性。針對地表變形，本研究透過 2016 年美濃地震的 InSAR 同震位移、RTK-GPS 所測得的同震變形資料及長期地形特徵來分析潛在的地表活動構造。針對深處地殼變形，則使用 2016 年美濃地震餘震序列的重定位結果、震源機制解與地下速度模型來分析深處地下構造特性。

研究結果顯示關廟地區於美濃地震的線性同震變形特徵符合當地地形特徵，可能為潛在的淺層活動構造。該活動構造在美濃地震時被觸發而產生錯動，暗示其對於鄰近的地震活動可能十分敏感。地震學分析結果得到美濃地震的餘震序列可以分為三群。其餘震序列分別位於關廟—龍崎地區、主震附近以及主震北方約五公里處，震源深度分別為約 20-30 km、10-20 km 及 7-15 km。

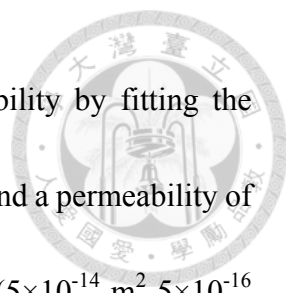
此外，美濃地震餘震序列大多位於速度構造上高 V_p/V_s 比值的邊緣，其餘震分布模式可能受到地殼中的高液壓區影響。透過餘震的時空遷徙分析，餘震遷徙模式和深部地殼的液體擴散方向有高關聯性。推測是 2016 年美濃主震所造成的斷層滑移使得應力移轉、鄰近地殼液壓改變，造成液體放射狀向外擴散，並在主震周圍引發了團狀、擴散半徑約為 4 km 的餘震群。這種非位於隱沒帶、火山地熱區的中深部地殼（深度可達到 18 km）液體擴散行為十分罕見。透過庫倫應力移轉分析及地殼滲透率的估算，本研究得出美濃主震附近岩體處於伸張應變量的環境，且滲透率約為 $3.36 \times 10^{-14} \text{ m}^2$ ，落在所謂的 seismogenic permeability 的區間 ($5 \times 10^{-14} \text{ m}^2$ - $5 \times 10^{-16} \text{ m}^2$)。根據上述結果，本研究推測 2016 年美濃地震所造成的破裂面造成了伸張的裂隙，使得原本儲存於裂隙中的液體擴散出去，造成鄰近地區液壓提升，瞬間達到 seismogenic permeability 的區間，因而產生團狀分佈的餘震。由滲透率和餘震擴散半徑來估算，美濃地震驅動了體積約 $7.22 \times 10^9 \text{ m}^3$ 的液體流動。該大規模的液體流動現象對於台灣西南部造山帶前緣的深處地殼變形有顯著性的影響。

關鍵字：美濃地震、液體擴散、泥岩區、斷層、滲透率

Abstract



This study integrates geodetic observations, topographic analysis and seismic methods to constrain the characteristics of active tectonics in the Guanmiao-Meinong area in southern Taiwan. I use coseismic displacements of the Meinong earthquake derived from InSAR, red relief image map (RRIM) and RTK-GPS measurements for topographic analysis and mapping active structures. On the other hand, I relocate aftershocks and calculate their focal mechanisms to infer structural architectures at deeper depths. The results show that two lineaments active during the Meinong earthquake fit topographic features, implying multiple seismic events, and deeper seismogenic structures are located at the boundary of high V_p/V_s area, which high fluid pressure is implied. The spatiotemporal aftershock migration analysis shows that the partial aftershock sequence is driven by fluid diffusion process. The pore fluid pressure has profound influence on earthquake initiation and has been widely observed in geothermal and injection-induced earthquake activities at shallow crustal depths, but rarely exceeding 10 km in depths. However, the mid-to-lower crustal fluid flow triggered by the 2016 M_w 6.4 Meinong earthquake is located at as deep as 18 km. Moreover, the spatiotemporal distribution of these fluid-driven aftershocks mainly spreads outward spherically from the Meinong mainshock with a radius about ~ 4 km. To quantitatively verify whether the fluid flow could occur at such mid-to-lower crustal depths, I calculated the Coulomb stress transfer



due to the Meinong earthquake and estimated the in-situ permeability by fitting the aftershock migration rate. Both show the positive dilatational strain and a permeability of $\sim 3.36 \times 10^{-14} \text{ m}^2$ within a so-called seismogenic permeability range ($5 \times 10^{-14} \text{ m}^2 - 5 \times 10^{-16} \text{ m}^2$) in the aftershock area. It is inferred that the rupture on the fault of the Meinong earthquake results in the dilatational cracks within the overlying over-pressured fluid reservoir, and in turn promotes the permeability to a transient seismogenic value. This disturbance then causes the pore pressure change and triggers the aftershocks with a spherical distribution following the fluid migration front. A total fluid volume of about $7.22 \times 10^9 \text{ m}^3$ to cause such fluid migration distance is required to exist in the pore space, which provides an important constraint on crustal fluid flux estimation.

Key words: Meinong earthquake, fluid diffusion, mudstone, fault, permeability

目 錄



口試委員會審定書.....	i
謝辭.....	ii
中文摘要.....	iii
Abstract.....	iv
Chapter 1 Introduction.....	1
1.1 Motivations.....	1
1.2 purpose.....	1
Chapter 2 Study Area.....	3
2.1 Active tectonics in southwestern Taiwan	3
2.1.1 Geology background of southern Taiwan.....	3
2.1.2 Geodesy observations.....	4
2.1.3 Geodesy observations.....	4
2.1.4 Stratums in southern Taiwan.....	5
2.2 The 2016 Meinong earthquake.....	6
Chapter 3 Methods.....	11
3.1 Geodesy methods.....	12
3.1.1 InSAR.....	12
3.1.2 RTK-GPS.....	13

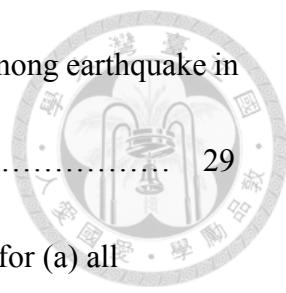
3.1.3 Red relief image map.....	13
3.2 Seismology methods.....	13
3.2.1 Earthquake clustering.....	13
3.2.2 Earthquake relocation.....	14
3.2.3 Focal mechanism determination.....	15
3.2.4 Earthquake migration analysis and permeability calculation...	15
3.2.5 Fluid volume estimation.....	18
3.2.6 Coulomb stress analysis.....	19
Chapter 4 Results	20
4.1 Topographic Analysis.....	20
4.2 Seismology Analysis.....	24
Chapter 5 Discussion.....	30
5.1 Shallow active structures.....	30
5.2 Relation between Fluid diffusion and aftershock migration.....	30
5.3 Insights from shallow and deep structures.....	40
Chapter 6 Conclusion.....	41
Reference.....	42



圖目錄



Figure 1 InSAR results from Huang et al. (2016)	8
Figure 2 Fault slip distribution and schematic interpretation of slip triggering from Huang et al. (2016).....	9
Figure 3 Research procedure.	12
Figure 4 Spatiotemporal earthquake evolution for the three aftershock clusters of the Meinong earthquake (a-c) and the Jiashian earthquake sequence (d).....	17
Figure 5 Spatiotemporal evolution of the fluid-driven aftershocks in map view (left) and along the N-S profile AA' (right).	19
Figure 6 Pseudo vertical (A) and E-W (B) displacements of coseismic deformation.	21
Figure 7 N-S and E-W topographic profiles of the bulge.	22
Figure 8 The topographic profile in Guanmiao town (profile A-A') and the elevation measured by RTK-GPS (Profile B-B' and C-C').	22
Figure 9 Topographic profiles in the Shenkeng Village area (the upper panel) and topographic profiles.	23
Figure 10 Relocated aftershock distribution, focal mechanisms, and velocity model.	26
Figure 11 Relocated aftershock distribution, focal mechanisms, and velocity model in map view and in four cross sections (AA'-DD').	27
Figure 12 Background seismicity distribution in 2012-2016 (top), typical aftershocks	



(middle) and fluid-driven aftershocks (bottom) of the Meinong earthquake in the cross sections AA' and BB', respectively. 29

Figure 13 Temporal frequency of the central aftershock cluster and for (a) all aftershocks, (b) remaining aftershocks, (c) and fluid-driven events. 33

Figure 14 Coseismic Coulomb stress and strain changes of the Meinong earthquake at different depths. The finite fault model is based on Huang et al. (2016)... 37

Figure 15 Aftershock distribution with coseismic dilatational strain change (a) and V_p/V_s structure (b) in the cross-section AA' of Fig. 10..... 38

Figure 16 Compiled crustal-scale permeability measurements from seismic and laboratory measurements in previous studies..... 39

Figure 17 The schematic interpretation from Maryline et al. (2017). 40

Chapter 1 Introduction



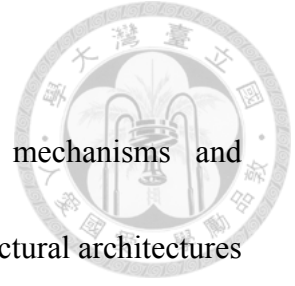
1.1 Motivations

Southern Taiwan which is located at the frontal fold-thrust belt of the western foothills is one of the areas with the most active tectonic movement and rapid topographic evolution in Taiwan (Ching et al., 2011). In recent years, several major earthquakes occur in Southern Taiwan such as the M_w 6.4 2010 Jiashian earthquake, the M_w 6.4 2012 WuTai earthquake and the 2016 M_w 6.6 Meinong earthquake. The 2016 Meinong earthquake caused 117 deaths, which is the second severe earthquake disaster in the past seven decades. However, both of these two earthquakes are triggered by blind faults, implying the potential active structures at depths beneath the frontal fold-thrust belt of the western Foothills in southern Taiwan. Besides, the coseismic deformation of the Meinong mainshock seems to be triggered by the potential lineaments (Huang et a., 2016). Therefore, this study aims to integrate the crustal deformation patterns both at shallower and deeper depths to explore the characteristics of active structures and the tectonic activities in southern Taiwan by using methods of geodesy and seismology.

1.2 Purposes

This study aims to achieve the following goals:

1. Map active structures on the surface.
2. Relocate the aftershock sequences, calculate their focal mechanisms and underground velocity model of P-wave and S-wave to infer structural architectures at deeper depths.
3. Inferring possible mechanisms of the aftershock migration and aftershock distribution patterns of the Meinong mainshock.



Chapter 2 Study Area

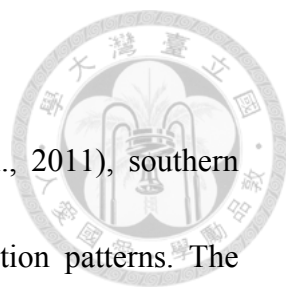


2.1 Active tectonics in southwestern Taiwan

2.1.1 Geology background of southern Taiwan

Southern Taiwan are located at the frontal fold-thrust belt of the western Foothills, and this orogenic region is in the initial stage of orogeny (Suppe, 1981). This region is one of the areas with the most active tectonic movement and rapid topographic evolution in Taiwan. The interseismic slip rate in southern Taiwan is up to 1 cm/yr (Ching, 2011). Because the Philippines Sea Plate is converging with the Eurasian Plate at 8 cm/yr in the west north west direction, most of the strike of active faults in southern Taiwan is Northeast-southwest trending (Seno et al., 1993). The active tectonic structures include the Hsinhua fault, the Lungchan fault, the Chishan fault, the Tsochen fault and the Hsiaokangshan fault (Chen et al., 2016). The Hsinhua fault is a right lateral fault with N70°E trending (Chen et al., 2016). The Lungchan fault is a reverse fault with Northeast-southwest trending (Chen et al., 2016). Its dipping angle is 70° ~ 80° in a direction of east. The Chishan fault is a reverse fault with northeast-southwest trending (Chen et al., 2016). The Tsochen fault is a left lateral fault with northwest-southeast trending. The Hsiaokangshan fault is a reverse fault with NNE trending (Chen et al., 2016).

2.1.2 Geodesy observations

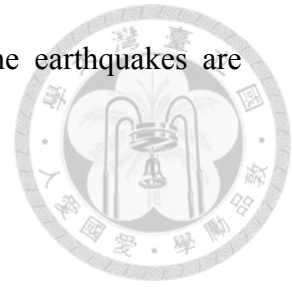


From GPS observations (Hsu et al., 2009; Ching et al., 2011), southern Taiwan area experiencing complicate and multiple deformation patterns. The velocity field at the Hsinhua fault moves in a direction of SSE (Hsu et al., 2009). The area near the Tsochen fault moves in a direction of left with the velocity about 12 mm/yr (Hsu et al., 2009). The GPS velocity increases from north to south. In the Chishan fault area, the velocity increases up to 50-55 mm/yr in a direction of southwest (Hsu et al., 2009). As for the strain rate observation, southern Taiwan area primarily is experiencing contraction rate about 0.5~1.5 μ strain/yr in a direction of E-W (Ching et al., 2011). The Tsochen fault, Chishan fault and Hsiaokanshan fault area are experiencing high NW to W-SE to E contraction about -1.4~-1.55 μ strain/yr (Hsu et al., 2009).

2.1.3 Seismology observations

Affected by active tectonic movements, it also has active seismic activities in southern Taiwan (e.g., Huang et al. 2000; Wu et al., 2008). From the historical seismic activity data (Wu et al., 2008), most of the epicenters of historical earthquakes are located around the adjacent active faults such as Hsinhua fault and

Chishan fault. In southern Taiwan, the source depths of the earthquakes are shallow (less than 30km).



2.1.4 Stratums in southern Taiwan

The main stratums in southern Taiwan includes Gutingkeng formation, Erchungchi formation, Liushang formation and Alluvium plain and tableland in chronological order of deposition.

Gutingkeng formation, which consists of mudstone, is one of the most widely distributed stratums in southern Taiwan (Ho, 1986). It deposits in Pliocene (Ho, 1986). The grain size of mudstone is extremely fine, so its permeability is relatively low. Besides, the rock strength of mudstone is weak. Therefore, it is easily to be eroded by the rain. Erchungchi formation, which distributes mainly around the upstream and midstream area of Erren River, deposits on Gutingkeng formation in Pleistocene (Chen, 2016). The lithologic character of upstream of Erren River is primarily sandstone and limestone. As for the midstream of Erren River, it primarily consists of thick sandstone interbedded with mudstone. Cuestas are the widely known landforms in this area (Chen, 2016). Liushang formation deposits on Erchungchi formation in the late Pleistocene (Chen, 2016). The lithologic character is mainly alternations of sandstone and shale. It mainly

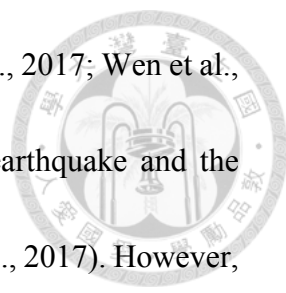
distributes in the west of the south Taiwan (Chen, 2016). Alluvium plain and tableland are the youngest strata in south Taiwan. The sediment in this area includes gravel, sand and clay (Chen, 2016).



Because of the widely distributed mudstone in south Taiwan, mud diapir plays an important role on crustal deformation. Due to the rapid deposition in the deep sea environment, the water in the pore of sediment is hardly to discharge totally. The gravity of the upper sediment rises up the pore fluid pressure of the lower muddy sediment, causes the overpressure phenomenon in the rock formations. The overpressure muddy sediment is easily extruded by faulting, causing the arched strata (Sun and Liu, 1993). Diapiric anticlines are widely distributed in the offshore Tainan-Kaohsiung-Hengchun area (Liu et al., 1995).

2.2 The 2016 Meinong earthquake

On February 5, 2016, the M_w 6.4 Meinong earthquake occurred beneath the frontal fold-and-thrust belt of the southwestern Taiwan with a focal depth of ~16 km (Huang et al., 2016; Kanamori et al., 2017). Its focal mechanism is 295° , 30° , and 37° in strike, dip, and rake (Kanamori et al., 2017; Wang et al., 2017), similar to that of nearby 2010 Jiashian earthquake (Huang et al., 2011). The mainshock fault of the Meinong earthquake is a blind fault which is located in the area among Tsochen fault and Chishan



fault with an ES-WN trending and dipping toward north (Wang et al., 2017; Wen et al., 2017). Some research regards that the ruptures of the Meinong earthquake and the Jiashian earthquake are located on the same fault system (Wang et al., 2017). However, the aftershocks and the surface displacement exhibit complex pattern distinct from those of the Jiashian earthquake. First, the maximum horizontal and vertical coseismic displacement occur in Guanmiao-Lungchi area, especially near Lungchuan fault area (Figure 4), which is far from the epicenter Meinong (Huang et al., 2016). The abnormally significant uplift is considered to be induced by the mud diapir because the Lungchuan fault is located at the mudstone area with high fluid pressure (Huang et al., 2016). Second, deformation patterns of the Meinong earthquake in the shallower crust is different from that in the deeper crust (Figure 5). The slip patterns of the fault planes at shallower depths and the mainshock fault at the depth of 16 km are not similar (Huang et al., 2016). It indicates that the dislocation patterns of the 2016 Meinong mainshock is multiple at different depths. The unusual deformation patterns in the Meinong earthquake suggest the complexity of the structures architectures in frontal fold-thrust belt of southwestern Taiwan.

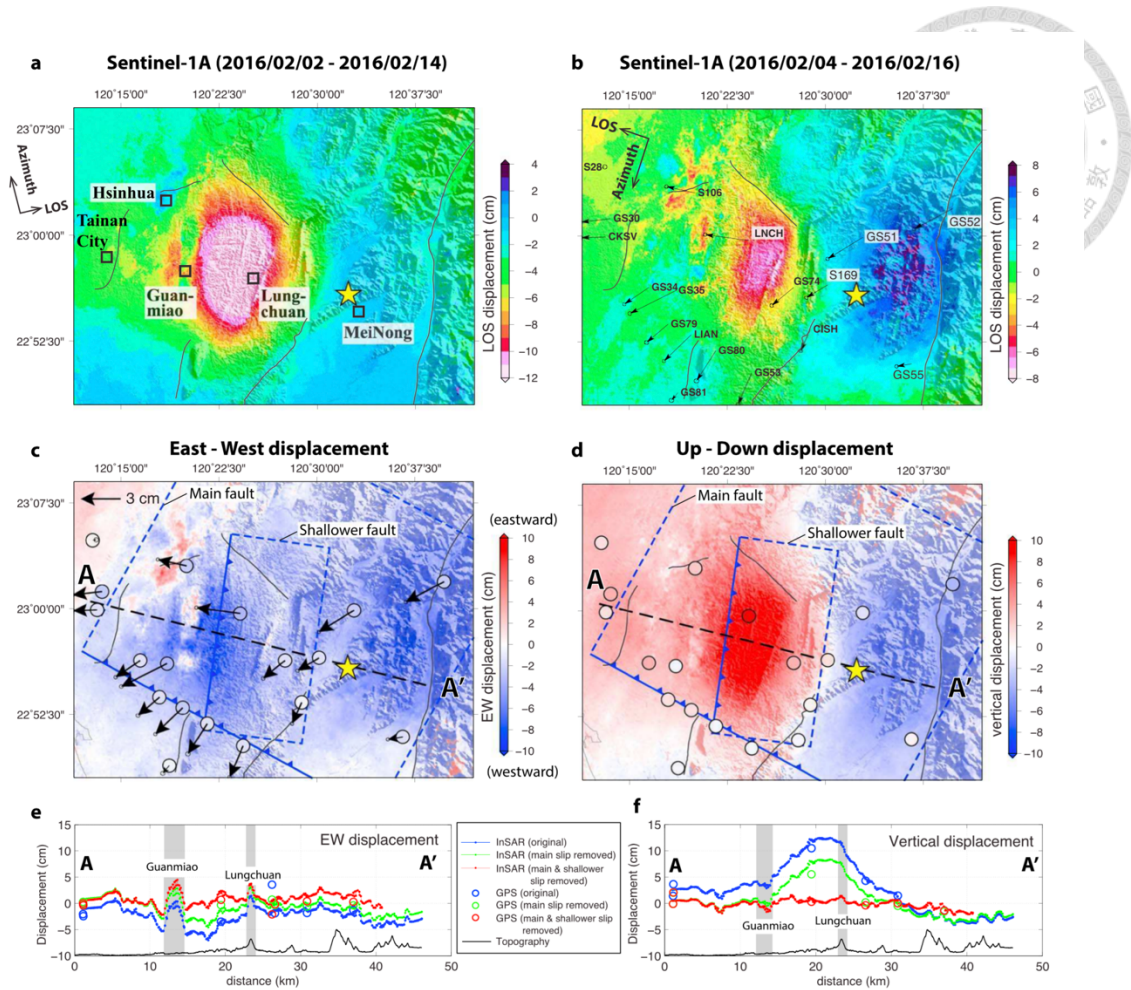


Figure 1 InSAR results from Huang et al. (2016). (a) Ascending and (b) descending Sentinel-1A interferograms. The warm and cold colors represent range decrease and increase of LOS displacement, respectively. The arrows in the map view are coseismic displacement derived from GPS measurements, and the black lines are active faults in the research area. (c) The east-west and (d) vertical displacements calculated based on (a) and (b). The dashed blue lines are the surface projection of the two inferred faults. (e) Cross section of E-W and (f) vertical displacements along profile AA' in (c) and (d). The blue, green, and red colors are the original displacement, displacement without

main slip contribution, and displacement without main slip as well as shallow slip contributions, respectively.

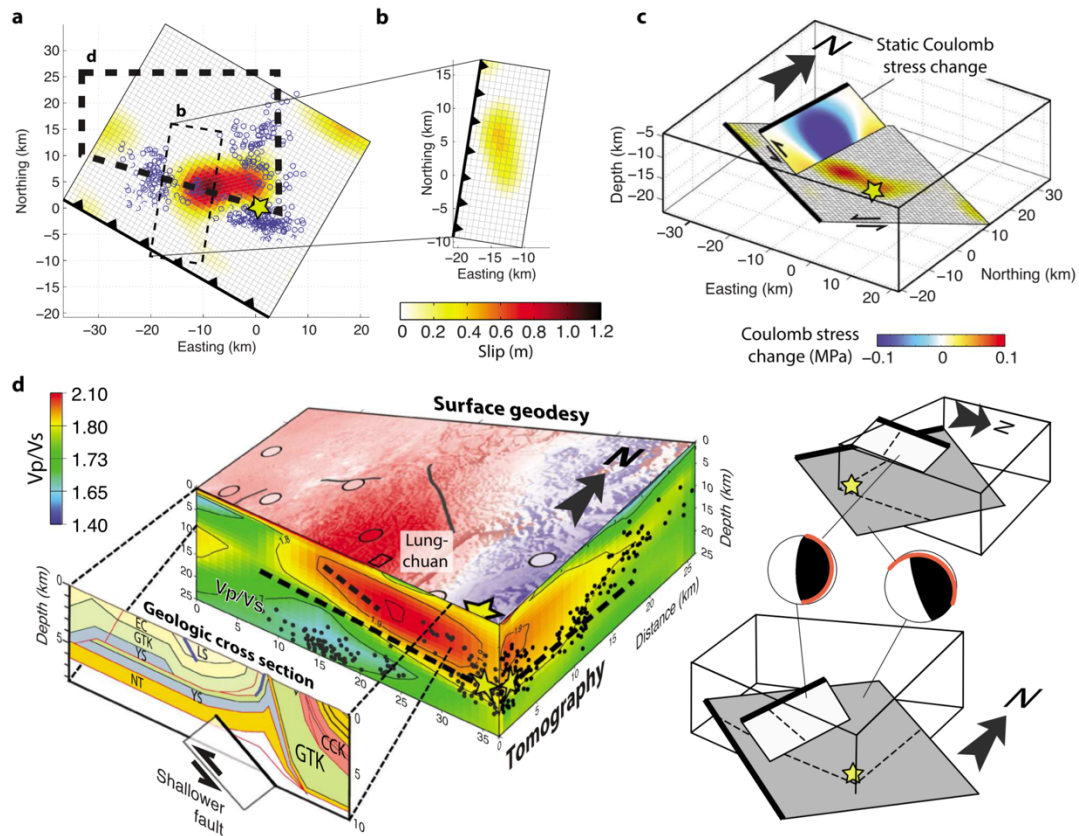
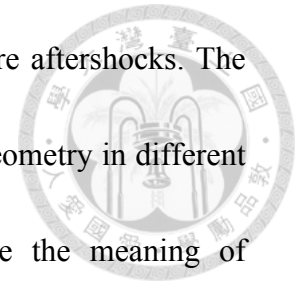


Figure 2 Fault slip distribution and schematic interpretation of slip triggering from Huang et al. (2016). Map view of slip distribution on (a) the main fault and (b) the shallower fault. The blue circles in (a) are aftershocks. The white-to-red color bar in (a) and (b) indicates the amount of slip. (c) Three day slip of the main and the shallower faults. The colors on the fault plane are the static Coulomb stress change due to slip on the main fault. (d) The cross sections are the V_p/V_s ratio and the geologic cross section along profile A-A' in Figure 4c. In the V_p/V_s ratio cross sections, the yellow star is the

earthquake hypocenter of Meonong mainchock. The black dots are aftershocks. The minor 3-D figures in the right panel represent the inferred faults geometry in different perspectives. In the geologic cross section, the followings are the meaning of abbreviations: LS-Holocene; EC-Early Pleistocene; YS-Late Pliocene; NT-Middle Pliocene; GTK-Pliocene to Early Pleistocene; CCK-Late Miocene. The blue lines in the geologic cross section show inferred very shallow fault slip that corresponds to surface ruptures.



Chapter 3 Methods



This study aims to analysis active the characteristics of active structures and tectonic activities associated with the Meinong earthquake at the shallow and deep depths. Figure 1 is the procedure of this research. Aiming at the surface deformation, this study focuses on the deformation features of the tectonic structures on the surface. I map active structures on the surface by using coseismic displacements of the Meinong earthquake derived from InSAR and using red relief image map (RRIM) and RTK-GPS to analyze the tectonic structures and its potential movement. On the other hand, I use the methods of seismology to analyze the deformation at the deep crust. I relocate the aftershock sequences, calculate their focal mechanisms and underground velocity model of P-wave and S-wave to infer structural architectures at deeper depths. Next, this study infers the mechanisms inducing the aftershock migration through the spatial-temporal patterns of aftershocks and calculate the Coulomb stress. And Last, this study integrates the results above to infer the possible mechanisms having influences on tectonic movement and the tectonic characteristics in southern Taiwan.

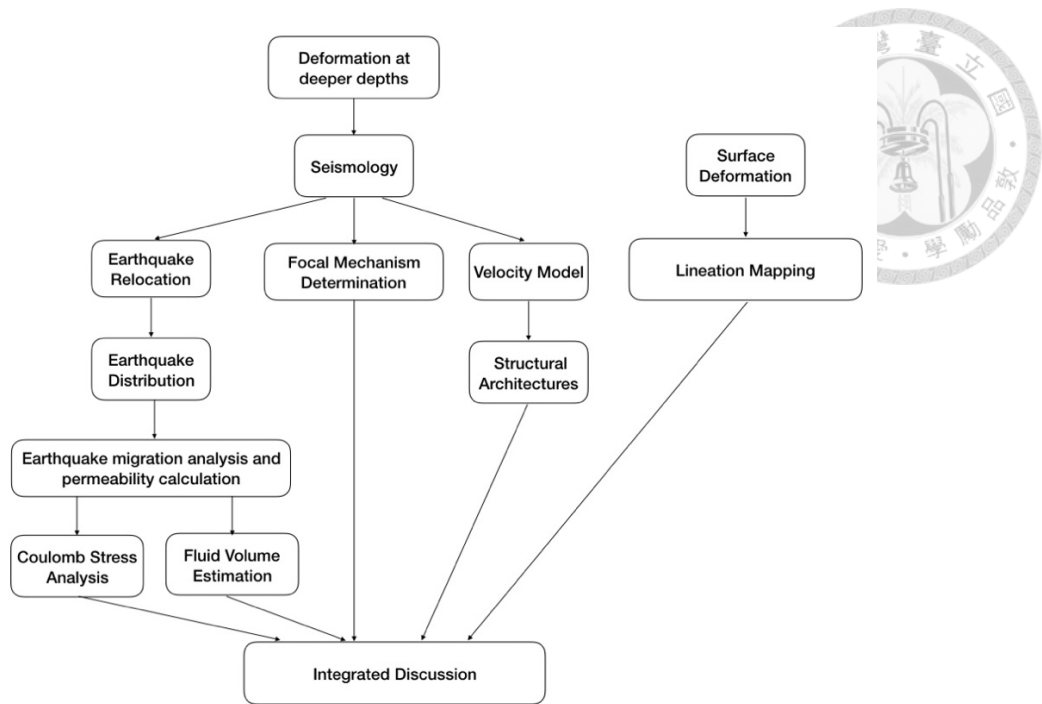
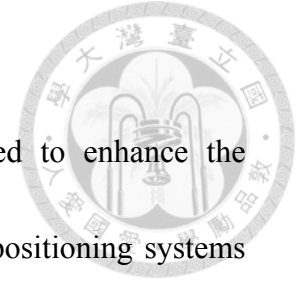


Figure 3 Research procedure.

3.1 Geodesy methods

3.1.1 InSAR. Interferometric synthetic aperture radar (InSAR) is a method to obtain the high-accuracy DTM (Vachon et al., 1996). It has the advantages that it doesn't affected by the weather and that it can shoot large-area surface (Vachon et al., 1996). It calculates the 3-D displacement and position of the landforms through the phase differences and Doppler effect of the interferograms derived from different periods (Vachon et al., 1996). The surface deformations can be obtained by calculating the difference in two periods. This study uses four ALOS-2 InSAR images to generate two ascending and two descending coseismic interferograms.

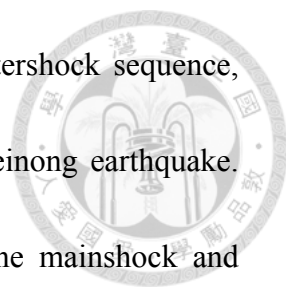


3.1.2 RTK-GPS. Real Time Kinematic (RTK) is used to enhance the precision of position data derived from satellite-based positioning systems such as GPS. It consists of a satellite receiver and a stock. Put the RTK on the ground vertically, it can calculate the precise x, y, z coordinate of the landforms in the real time.

3.1.3 Red relief image map. This study uses red relief image map (RRIM) to recognize the potential active tectonics on the surface. Red relief image map calculates the negative openness and positive openness of the subsidence and arched land features, respectively (Yokoyama, 2002; Chiba, 2008). Then it calculated the value $(\text{positive openness} - \text{negative openness})/2$ to distinguish the different land features such as hills and valleys with the red color bar (Yokoyama, 2002; Chiba, 2008). Compare to the traditional hill shade images, red relief image map has the advantage that it is shade-free 3D image. Therefore, it is better to recognize the boundary of the lineaments.

3.2 Seismology methods

3.2.1 Earthquake clustering. I use the double-link method (Davis and



Frohlich, 1991; Wu and Chiao, 2006) to extract the aftershock sequence, which has high spatiotemporal correlations with the Meinong earthquake. The thresholds of time and space distances between the mainshock and aftershocks are empirically chosen as 2 days and 4 km. Increasing the thresholds mainly links aftershocks that are farther away and does not change the pattern analyzed in the study.

3.2.2 Earthquake relocation. I relocate the extracted Meinong earthquake sequence with a modified double-difference earthquake relocation program (3D-DD), in which a single event location method for isolated events after double-difference pairing and a capability of incorporating three-dimensional velocity models are integrated into one scheme (Lin, 2014). A pseudo-bending ray tracing method (Um and Thurber, 1987; Koketsu and Sekine, 1998) in a three-dimensional spherical coordinate is used for travel time calculation. With a recent high-resolution velocity model in Taiwan (Huang et al., 2014), the 3D-DD scheme largely eliminates the path effect in earthquake relocation and the structural heterogeneity near sources, rendering the relocation a higher accuracy.

3.2.3 Focal mechanism determination. The focal mechanisms are determined by a first-motion method (Wu et al., 2008) with P-wave first-motion data collected from the seismic networks of Central Weather Bureau.

Wu et al. (2008) applied genetic algorithm (Goldberg, 1989) to obtain the best focal mechanism and estimate its uncertainty with a quality index, Q .

The solutions with ≥ 1 are used in the study.

3.2.4 Earthquake migration analysis and permeability calculation. The migration of earthquakes has been widely observed and can primarily be categorized into two mechanisms: afterslip-driven (Secor D. T., 1965) and fluid-driven (Shapiro et al., 1997). In the latter case, the spatiotemporal evolution of earthquakes follows the equation

$$r = \sqrt{4\pi t} \quad (1)$$

where r and t are distance (meter) and time (second) relative to mainshock, and D represents diffusivity (Shapiro et al., 1997). By fitting the group of fluid-driven aftershocks with the equation, I obtain $D = 2.1 \text{ m}^2/\text{s}$ (Fig. 1a, red dashed curve). To calculate the permeability, I follow the formula as

$$k = \frac{D\eta}{N} \quad (2)$$

D is derived from the earthquake migration fitting; η is assumed 0.001 for

water (Shapiro et al., 1997); and for low-porosity crystalline rocks N can be

$$\text{expressed as } N = \left(\frac{\phi}{k_f} + \frac{\alpha}{k_g} \right)^{-1}$$

where ϕ , k_f , and k_g are porosity, bulk moduli of the fluid and grain

material, respectively. It is a ratio between bulk moduli of the dry frame and

grain material and can be approximated as 0.03 in a low-porosity condition.

I adopt $k_f = 2.3 \times 10^{10}$ Pa and $k_g = 7.0 \times 10^9$ Pa from the hydraulic-fracturing

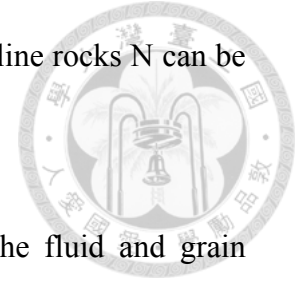
experiment in German Continental Deep Drilling Borehole (KTB) site

(Shapiro et al., 1997). Lastly, using the relation $V_p/V_s = 0.036 \phi^2 + 0.0178 \phi$

+ 1.79 (Um & Thurber, 1987) and the average V_p/V_s ratio of the fluid

reservoir (Figure 2b) from the tomography model (Huang et al., 2014), I

obtain ~2.7%. Taken together, I arrive at a permeability of 3.36×10^{-14} m².



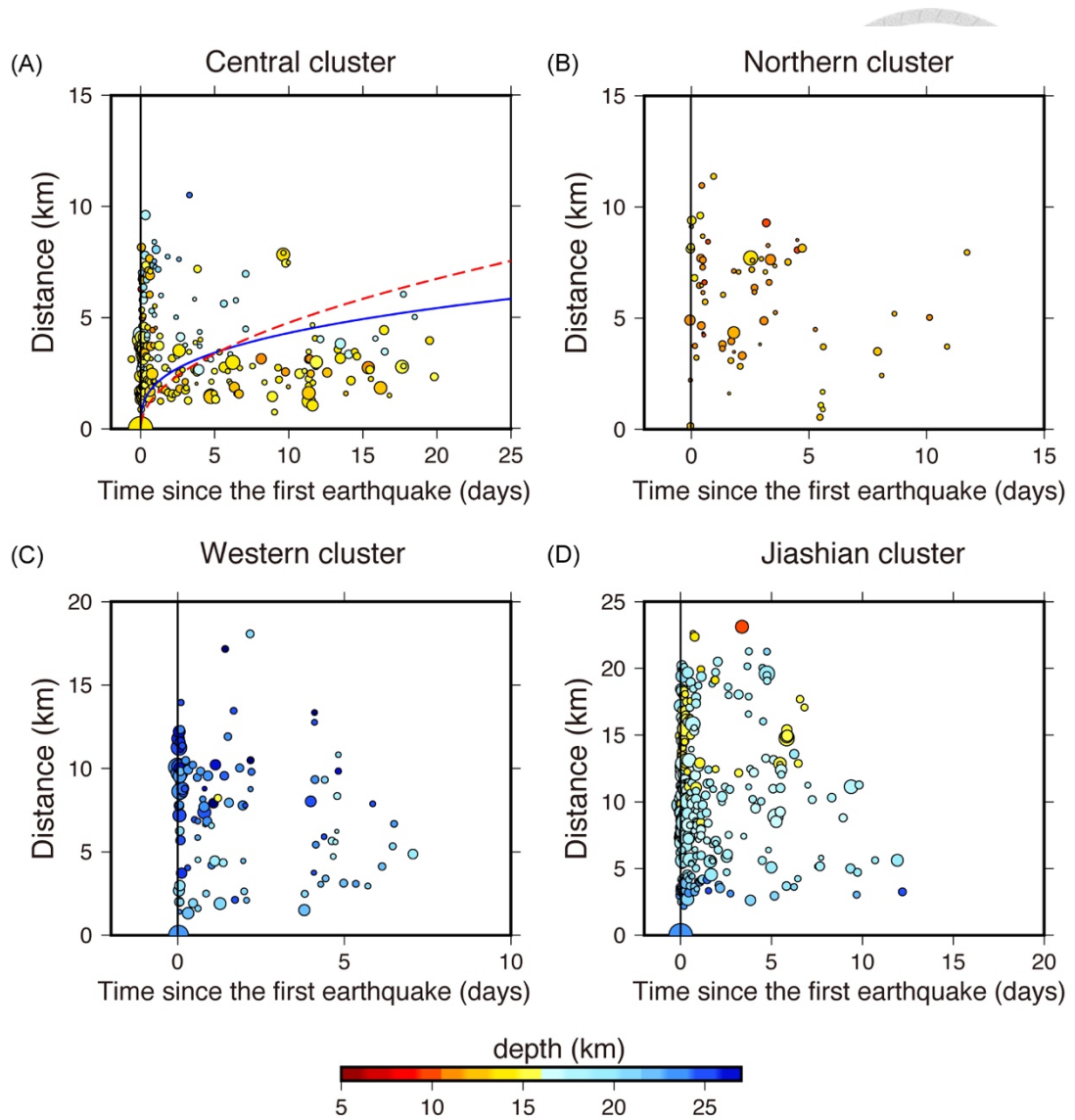


Figure 4 Spatiotemporal earthquake evolution for the three aftershock clusters of the Meinong earthquake (a-c) and the Jiashian earthquake sequence (d). The areas of central, northern, western and Jiashian cluster represent in the boxes A, B, C, and D in Figure 10, respectively. The black vertical lines denote the timing of the first event in the group. The red dashed and blue solid curves in (a) follow the square root and cubic root time, respectively. The color of each dot represents the depth of aftershocks.

3.2.5 Fluid volume estimation. Shapiro & Dinske (2009) further generalized the fluid-driven formula accounting for the nonlinear behavior of hydraulic fracturing, which can be expressed as

$$r = A(Q_I t / \varphi)^{1/3} \quad (2)$$

where Q_I and φ are the constant injection rate of the treatment fluid and fractured porosity, respectively. A is a dimensionless geometric factor equal to $1/2$ or $(3/4\pi)^{1/3}$ in the cases of cubic or spherical fractured domains. In this study, I used $A=(3/4\pi)^{1/3}$ as for observed radially spreading pattern (Fig. 3). φ is obtained as $\sim 2.7\%$ in previous section. $Q_I t$ is then the total fluid volume existing in the pore space to be estimated. I fit the group of fluid-driven aftershocks of the Meinong earthquake with equation (2) and obtain $Q_I t = 7.22 \times 10^9 \text{ m}^3$ for the hydraulic fracturing case (Fig. 2a, blue curve). The equation (2) gives a slightly better fitting than equation (1) (Fig. 2a).

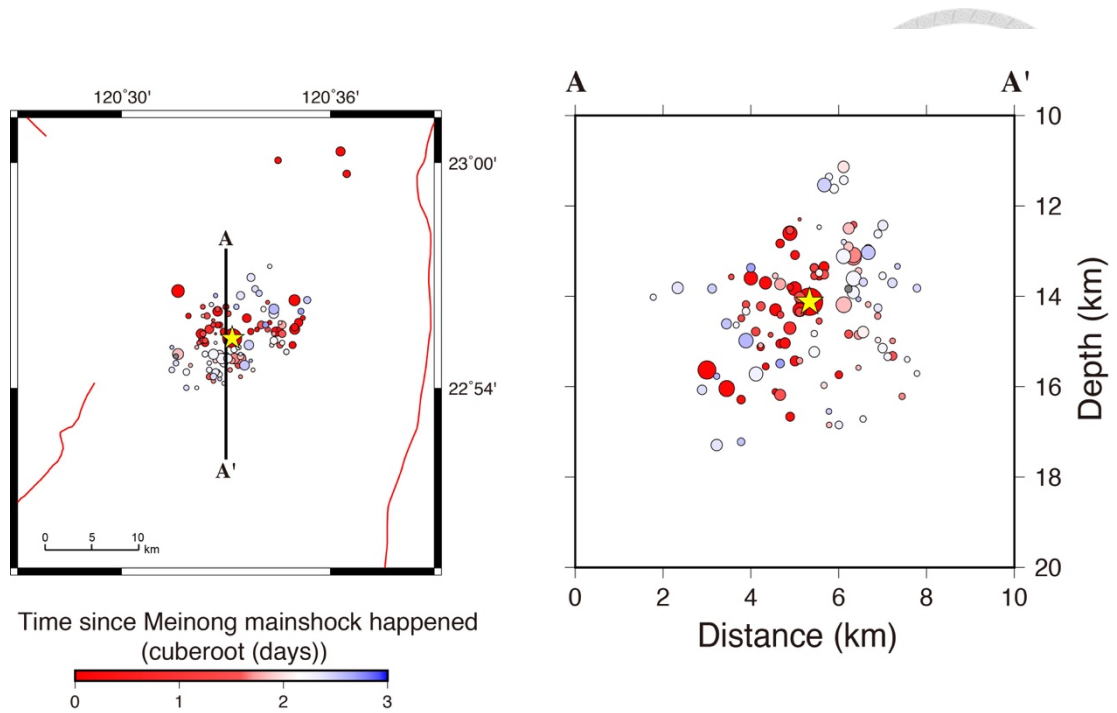
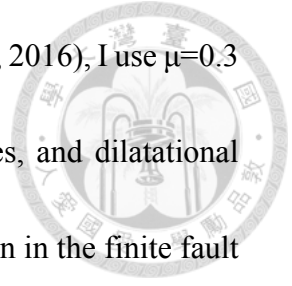


Figure 5 Spatiotemporal evolution of the fluid-driven aftershocks in map view (left) and along the N-S profile AA' (right). The dots are color coded by the cubic root of time after the Meinong mainshock in days. A generally radial spreading pattern can be observed.

3.2.6 Coulomb stress analysis. I use Coulomb 3.3 software to calculate the coseismic changes of stress and strain fields (Toda et al., 1998; Lin and Stein, 2004). The calculation principle of Coulomb 3.3 follows the Coulomb failure criterion $\Delta\sigma_f = \Delta\tau_s + \mu\Delta\sigma_n$, where $\Delta\sigma_f$ is the change of shear stress on the receiver fault caused by the slip on the fault of main shock, $\Delta\tau_s$ is the change of the shear stress, μ is the friction coefficient of the mainshock fault, and $\Delta\sigma_n$ is the change of the normal stress (Secor D. T., 1965). Based on a recent

finite fault model of the Meinong earthquake (Huang et al., 2016), I use $\mu=0.3$ to calculate the regional shear and normal stress changes, and dilatational strain, respectively. Note that since the mainshock location in the finite fault model is slightly different from my relocated one (~3 km apart), I shift the finite fault model to the relocated location accordingly.



Chapter 4 Results



4.1 Topographic Analysis

For the topographic analysis, I divide the Guanmiao area into three domains based on topographic features (Figure 6). In domain 1 (Figure 7), the green lineament is located on the boundary between the westward (cold color) and eastward coseismic displacement (warm color) from InSAR. The green lineament also fits the east side of bulge of Ming-du Chinpaoshan very well. I infer that the green lineament may be a potential active tectonic structure. The Meinong mainshock may trigger the dislocation of the green lineament. In domain 2 (Fig. 8), the RTK-GPS shows the significant coseismic displacement in the Guanmiao town (Fig. 8). Both of the coseismic uplift of green and purple lineaments are up to 50-60 cm. In domain 3 (figure 9), The topographic bulge of the green lineament extends to Erren River. The length of the potential active structure is about 20 km. The flow direction of the branch is also parallel to the lineament, implying that the flow direction of this branch may be controlled by this active structure. All of these lineaments derived from the topographic analysis play the important roles because they seem to be sensitive to the adjacent tectonic movement.

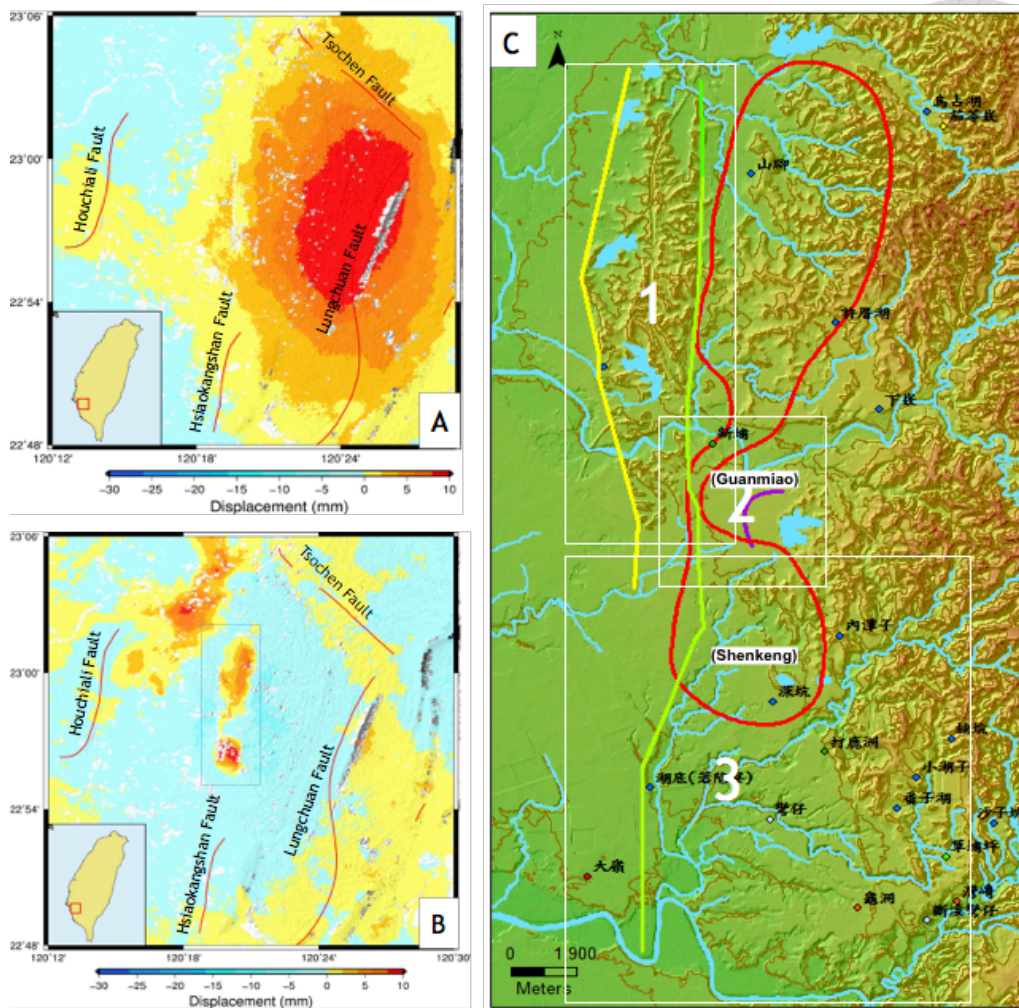


Figure 6 Pseudo vertical (A) and E-W (B) displacements of coseismic deformation. Red lines in (A) and (B) are major faults in the region. The right panel (C) indicates the area inside the red frame in (B). I divide (C) into three sections to describe the topographic features in this area. Red line in (C) represents the main coseismic deformation area.

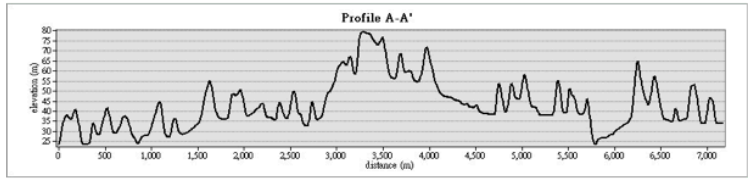
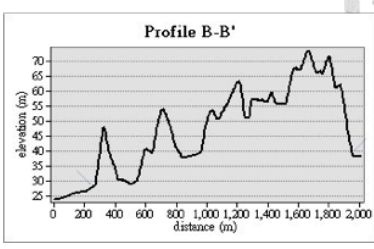
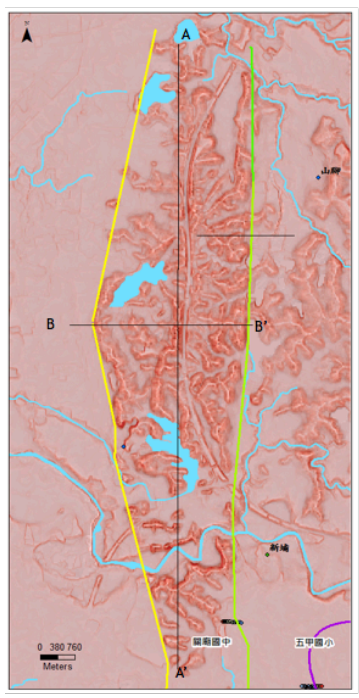
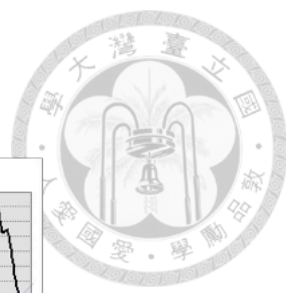


Figure 7 N-S and E-W topographic profiles of the bulge. The location of the profiles is in the left map. Blue arrows are inferred structural scarp. Profile B-B' shows the surface gradient is gentle dipping to the west.

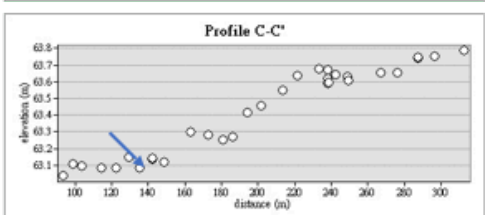
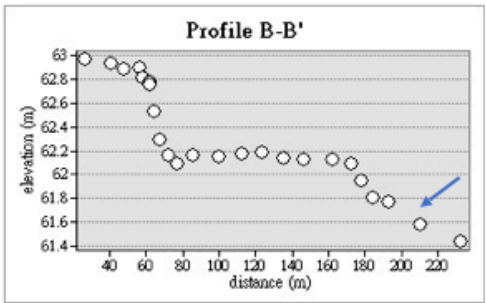
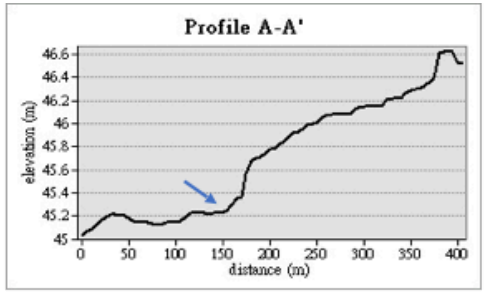
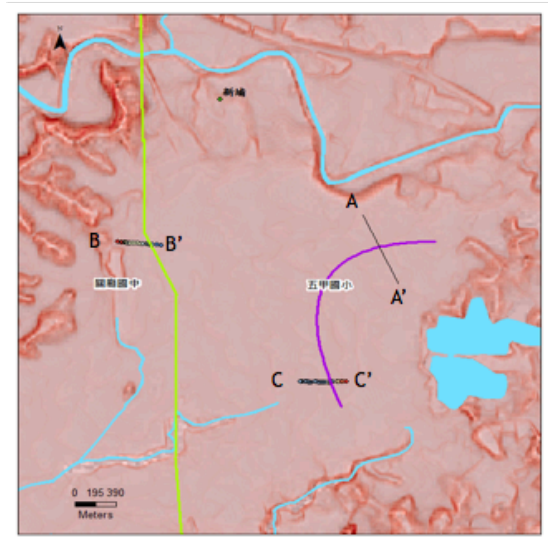


Figure 8 The topographic profile in Guanmiao town (profile A-A') and the elevation measured by RTK-GPS (Profile B-B' and C-C').

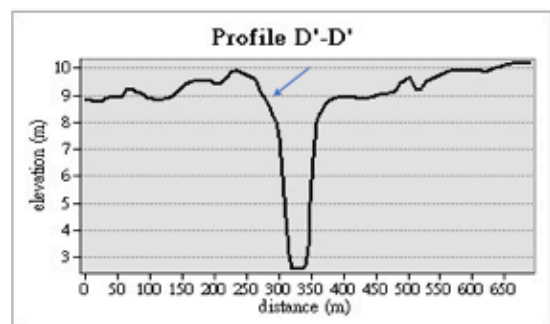
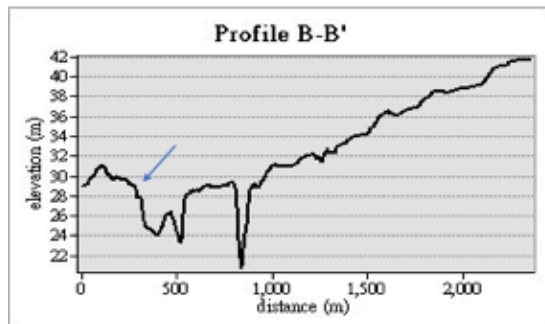
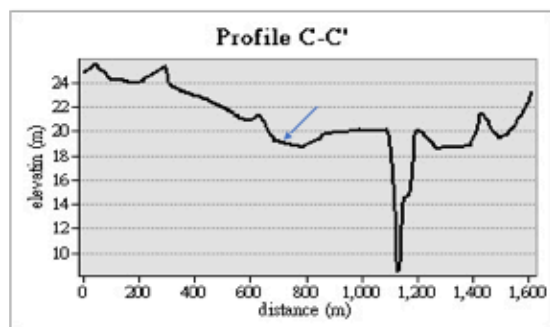
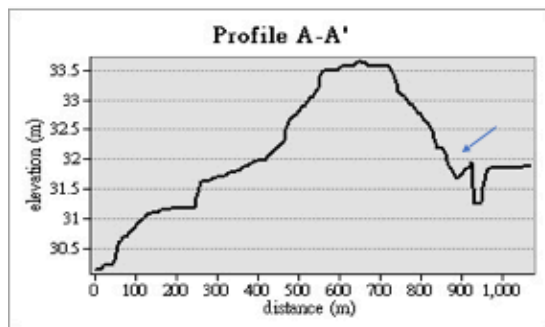
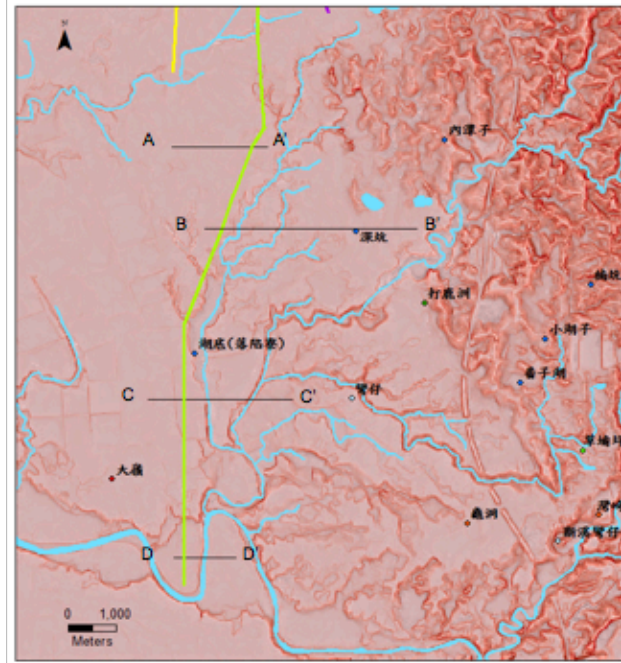
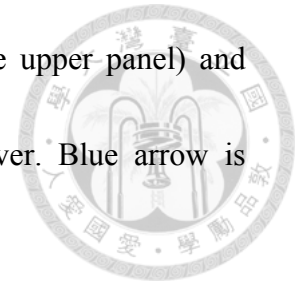
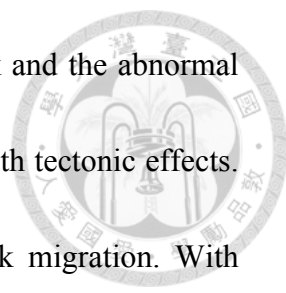


Figure 9 Topographic profiles in the Shengkeng Village area (the upper panel) and topographic profiles. The green lineament extends to Erren River. Blue arrow is inferred scarp of the lineament.



4.2 Seismology Analysis

By using a modified double-difference relocation method with a three-dimensional velocity model, the relocated mainshock-aftershock sequence shows three primary aftershock clusters in the west, north, and center of the mainshock (Fig. 10, boxes a, b, and c). For the northern cluster, the aftershocks are distributed sub-horizontally into two groups at depths of ~ 7 and ~ 11 km, well along the upper and lower boundary of a high V_p/V_s ratio anomaly (i.e. high Poisson's ratio) in a high-resolution velocity model (Huang et al., 2014) (Figure 10,11 and 12). For the central cluster, the aftershocks are also distributed around the lower boundary of the high V_p/V_s ratio area but is more scattered. The western cluster, which is deeper and ill separated from the other two clusters, is likely related to different structure and doesn't fit with the surface deformation patterns. Comparing the surface deformation pattern with the deformation pattern at the deep depth, I find out that the tectonic movements in the frontal fold-thrust belt of the western Foothills in southwest Taiwan are quite complex and can't be only explained by the movement of the active faults at shallow depth.



The non-linear aftershock distribution of Meinong mainshock and the abnormal spatial-temporal distribution are hardly to be interpretation only with tectonic effects. Therefore, I try to link the relation between fluid and aftershock migration. With earthquake migration analysis, I find evidence that part of the aftershock sequence is fluid-driven in a form of coseismic hydraulic fracturing in mid-to-lower crust. From the case of fluid-driven aftershock migration, I estimate a large fluid volume of 7.22×10^9 m³ existing in the lower crust and a permeability of $\sim 3.36 \times 10^{-14}$ m² that is three to four orders of magnitude larger than the long-term average (Manning, C. E. & Ingebritsen, S. E., 1997; Shmonov, V. M. et al., 2003). This indicates a very high transient permeability at lower crustal depths and an important role of deep crustal earthquakes promoting large-scale fluid movements in the crust. Such large permeability fluctuations could be important in investigating crustal rheology, lithospheric water, carbon cycle (Ingebritsen, S. E. & Manning, 2002; Plumper, O. et al., 2017) and provides an important constraint on crustal fluid flux estimation.

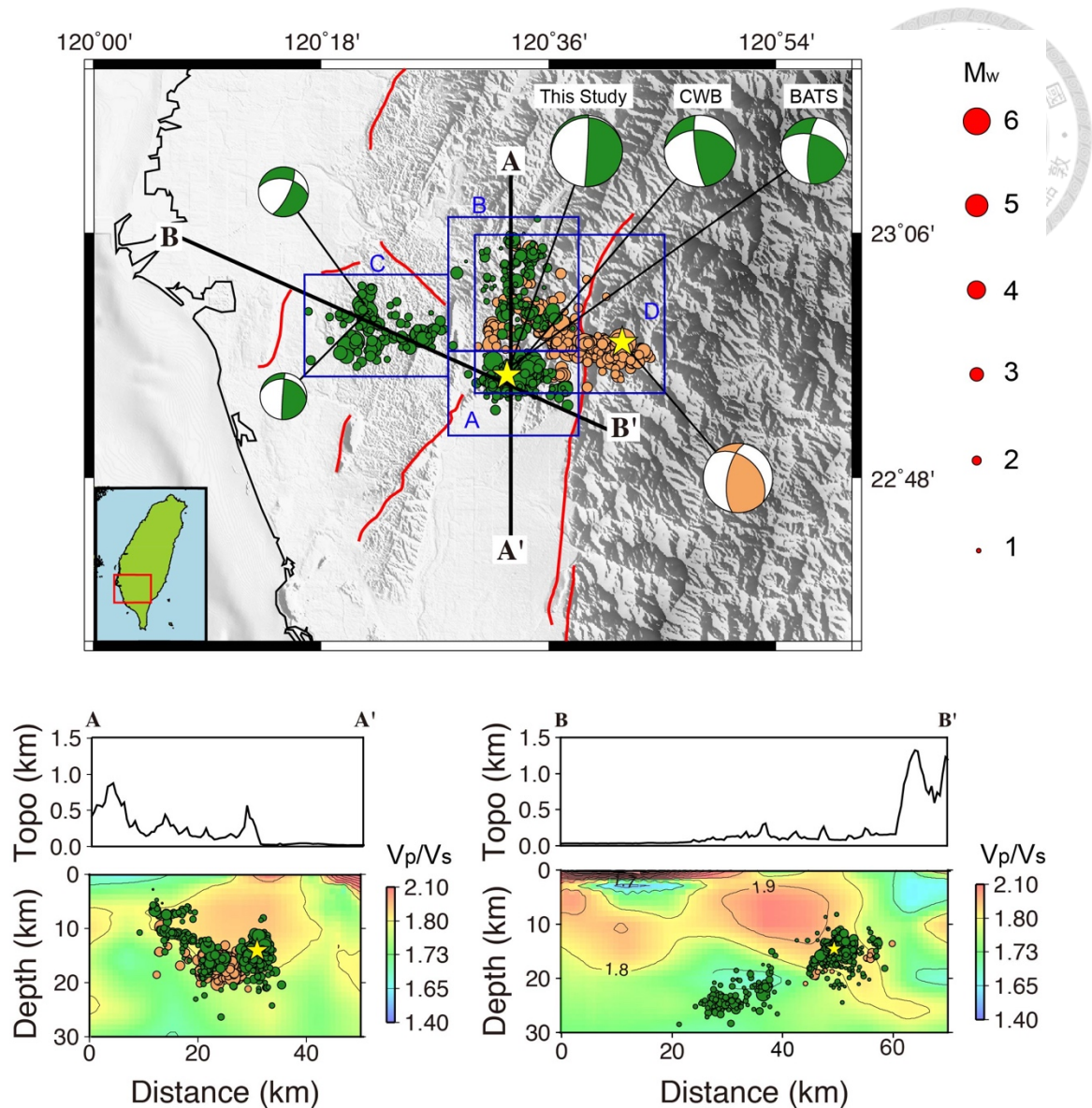
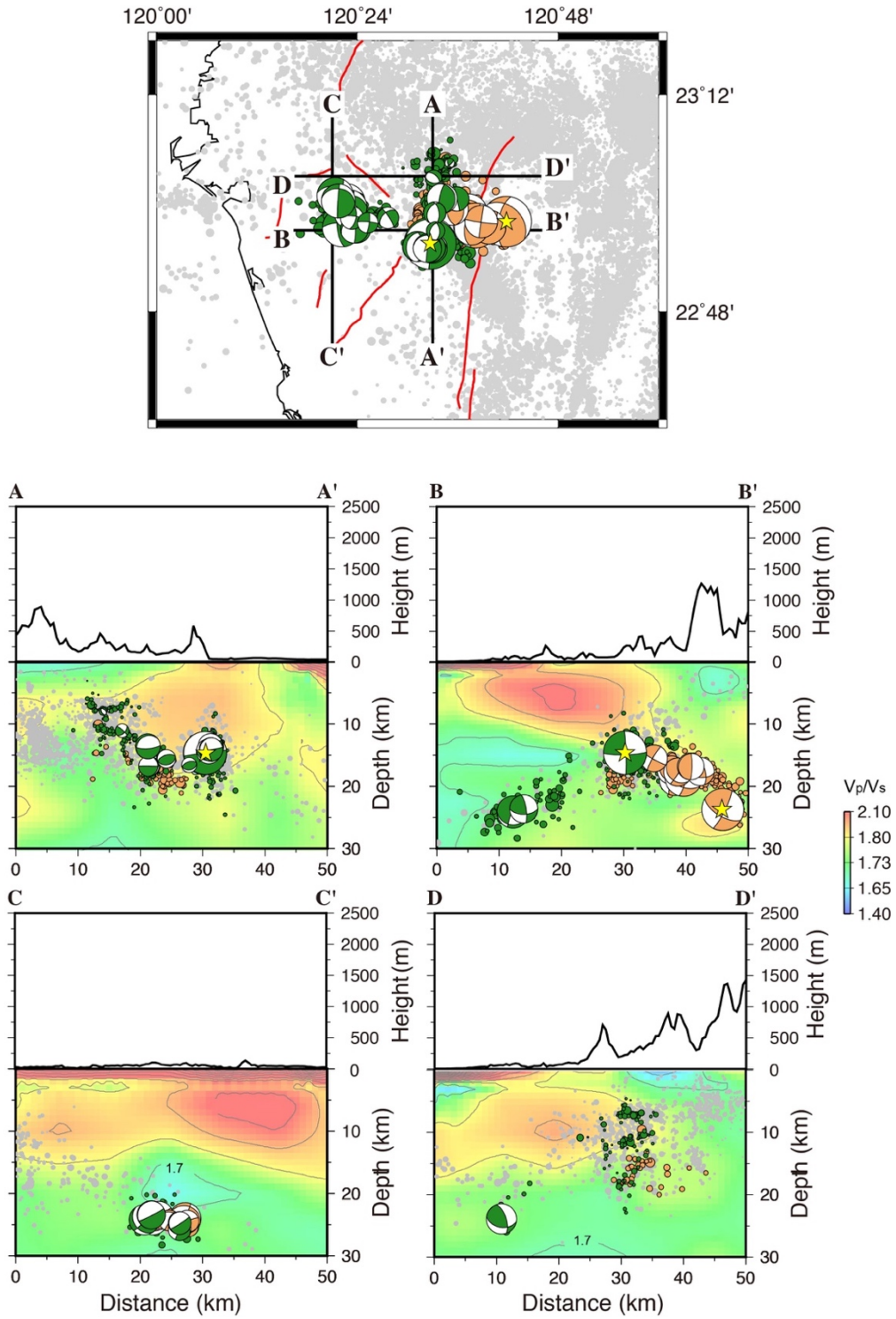


Figure 10 Relocated aftershock distribution, focal mechanisms, and velocity model.

Green and orange dots are the 2016 Mw 6.4 Meinong and 2010 Mw 6.2 Jiashian earthquake sequences, respectively. Yellow stars denote the hypocenters of Meinong and Jiashian earthquakes. The blue boxes divide the Meinong earthquake sequence into three clusters in Figure 2. Earthquakes within 5-km distance are projected on the cross sections. Black lines above the cross sections are topographic profiles with vertical

exaggeration of 10, and background colors are values of V_p/V_s ratio from Huang et al.

(2014).



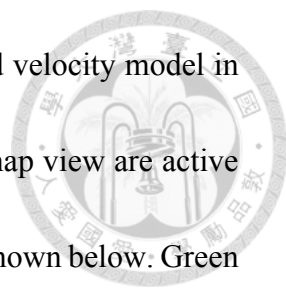


Figure 11 Relocated aftershock distribution, focal mechanisms, and velocity model in map view and in four cross sections (AA'-DD'). The red lines in map view are active faults and the black lines indicate the profile locations of AA'-DD' shown below. Green and orange dots are the 2016 Meinong and 2010 Jiashian earthquake sequences, respectively. Yellow stars denote the hypocenters of Meinong and Jiashian earthquakes. Earthquakes within 5-km distance are projected on the cross sections. Black lines above the cross sections are topographic profiles with vertical exaggeration of 10, and background colors are values of V_p/V_s ratio from Huang et al. (2014).

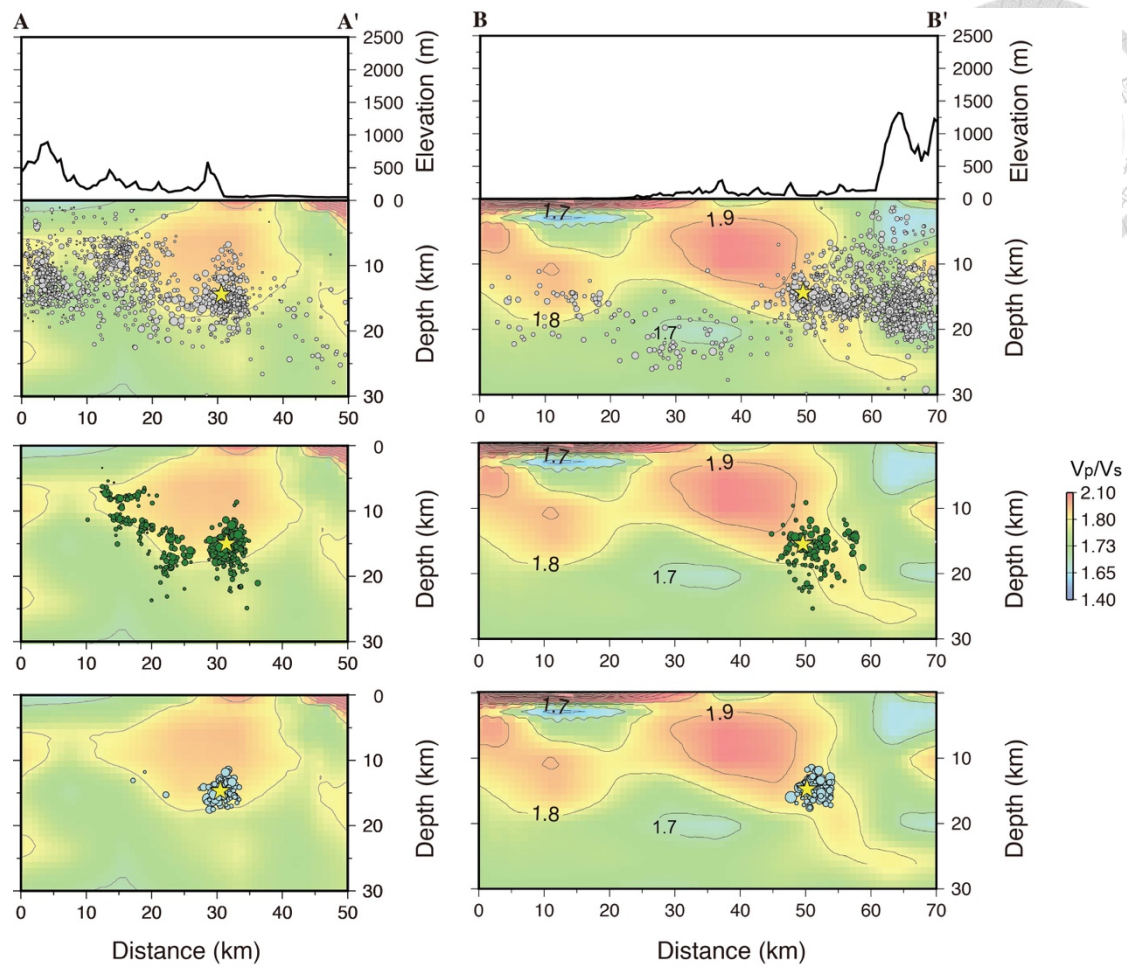


Figure 12 Background seismicity distribution in 2012-2016 (top), typical aftershocks (middle) and fluid-driven aftershocks (bottom) of the Meinong earthquake in the cross sections AA' and BB', respectively. The location of the cross sections is indicated in the Figure 10. Background color shows the V_p/V_s variation. Earthquakes within 5-km distance are projected on the cross sections.

Chapter 5 Discussion

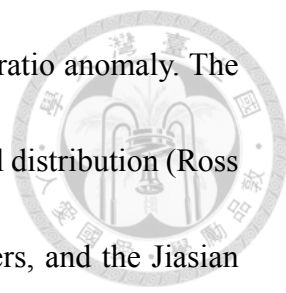


5.1 Shallow active structures

The vertical and horizontal displacement around Guanmiao town derived from InSAR results are similar with the GPS observations of Maryline et al (2017). The mapping results are also consistent with part of the study of Maryline et al (2017). The yellow and the green lineaments (Figure 6) may be corresponding to the Pitou anticline and Guanmiao syncline, respectively. The coseismic deformation of these two lineaments are corresponding to the long-term landform features. However, the deformation of Napalin anticline doesn't seem to be corresponding to the long-term landform features. Besides, the RTK-GPS results show a sharp coseismic subsidence occurring on the east side of the green lineament, which is consistent with the tension cracks caused by the coseismic displacement in Guanmiao town (Maryline et al., 2017). These field observations indicate that the Guanmiao syncline may be extended by the slip of Meinong mainshock.

5.2 Relation between Fluid diffusion and aftershock migration

Here, I focus on analyzing the spatiotemporal evolution of the central and northern



clusters, and their seismogenesis relationship with the high V_p/V_s ratio anomaly. The spatiotemporal evolution of the central cluster shows a clear bimodal distribution (Ross et al., 2017) distinct from those of the northern and western clusters, and the Jiasian earthquake sequence (Figure 2). For the long-lasting group of aftershocks, I can fit the long-lasting group of aftershocks with a square root time curve using a hydraulic diffusivity (D) as $2.1 \text{ m}^2/\text{s}$ (see Methods). If I extract only those aftershocks (below the red dashed curve in Figure 2a), they generally display a radially spreading pattern away from the mainshock with a radius about $\sim 4 \text{ km}$ (Figure 3). In addition, they do not show typical Omori law decay in frequency compared to the remaining aftershocks (Figure 13). By using finite fault model, I calculate the Coulomb stress transfer on shear stress, normal stress, and dilatation at different depths (Figure 14). The results show that the northern and a large portion of the central clusters mainly lie in the dilatational regimes where extensional cracks are likely to form (Figure 14). All these observations indicate in the center cluster a fluid-driven process is involved. I estimate the in-situ permeability k as $k = \frac{D\eta}{N}$, where D , N , η are hydraulic diffusivity of $2.1 \text{ m}^2/\text{s}$, pore-fluid dynamic viscosity and poroelastic modulus, respectively (Shapiro et al., 1997). Assuming low-porosity crystalline rocks at the depth of the mainshock, I estimate $\sim 6.2 \times 10^{10} \text{ Pa}$ and $\sim 0.001 \text{ Pa}\cdot\text{s}$ (see Methods). I then obtain permeability $\approx 3.36 \times 10^{-14} \text{ m}^2$. This value lies in the range of so-called seismogenic permeability (Talwani et al.,

2007), k_s (5×10^{-14} - 5×10^{-16} m²), meaning fluid flowing through the porous medium with $k=k_s$ can induce earthquakes, otherwise with less or more than it is aseismic.

Shapiro & Dinske (2009) proposed a generalized non-linear diffusional equation to account for a wide range of fluid processes including the linear fluid diffusion and hydraulic fracturing as two end-member mechanisms. The former shows square-root-time evolution and unilateral propagation of earthquake migration; the latter that is related to creation of new pore (fracture) volume has a rather cubic-root-time evolution and a radial growth in dimension for earthquakes (Shapiro et al., 2009). The data show a radial spreading pattern (Figure 3) and a slightly better fit to the cubic root parabola (Figure 2, blue curve), which is uniquely consistent with the hydraulic fracturing case. This suggests that the Meinong mainshock acts as a strong pressure source like an injection source in hydraulic fracturing experiments but at the depth of ~15 km. In this manner, since the injection volume can be related to the distance of the fluid triggering front (see Methods), I can then calculate how much of fluid will be needed (“injected” by the mainshock) to make the fluid front spread away as far as 4 km in radius (Fig. S2). The calculation shows that a total fluid volume of about 7.22×10^9 m³ which must store in the pore space around the mainshock area before rupture is required (See Methods). This is a huge volume two orders of magnitude greater than the cumulative water volume among biggest injection experiments (Keranen et al., 2013; McGarr et al.,

2014) and five orders of magnitude greater if only counting the hydraulic fracturing experiments (Gallegos et al., 2014), indicating a very fluid-rich mid-to-lower crust in the southwestern Taiwan. Another striking feature is that most of the aftershocks in the northern and central clusters locate along the high V_p/V_s boundary (Figure 10b, 11 and 12). Recent laboratory experiments suggested that the friction rate parameter ($a - b$) can change from velocity strengthening to velocity neutral behavior and favor stable sliding by the increase of pore fluid pressure (Ikari et al., 2013; Scuderi et al., 2016; French et al., 2017). For the center of the fluid reservoir where the pore pressure is supposed to be the highest may therefore be prone to the aseismic sliding during the coseismic disturbance. This gives a good explanation of why the aftershocks mostly only occur along the reservoir boundary, where the fluid pressure is high, but not yet enough to turn the friction state into stable sliding mode. In fact, I observe very low seismicity inside the high V_p/V_s area in the past decade (gray dots in Figure 11 and 12).

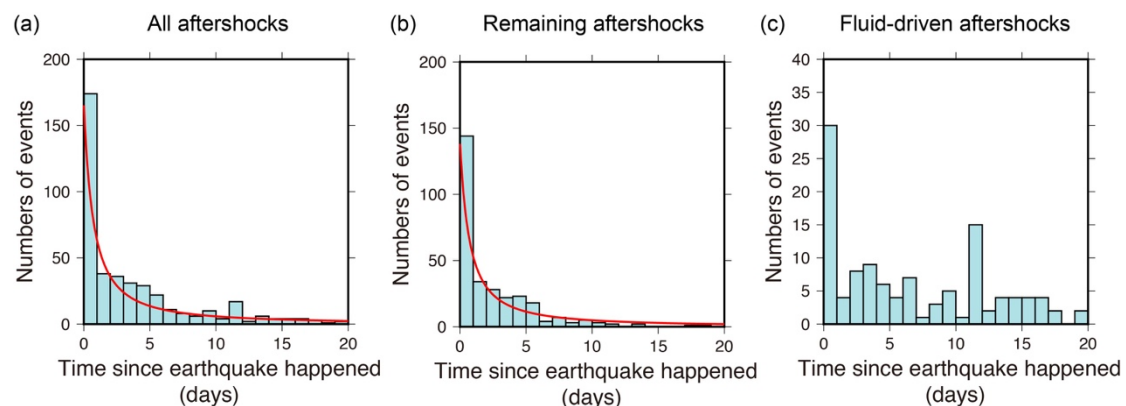
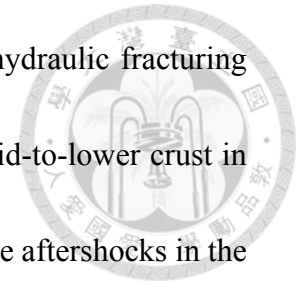
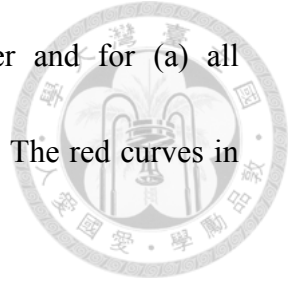
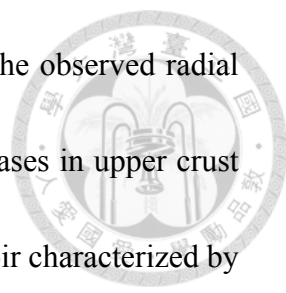


Figure 13 Temporal frequency of the central aftershock cluster and for (a) all aftershocks, (b) remaining aftershocks, (c) and fluid-driven events. The red curves in (a) and (b) show the best fitting with Omori's law



$$N(t) = \frac{C_1}{(C_2+t)^p}$$
$$C_1$$
 in (a) and (b) are 167.5 and 140, respectively. C_2 and p in (a) and (b) are 1 and 1.4, respectively.

Extension veins that are exhumed and observed along the ancient faults may be the most direct evidence of fluid associated with fault-fracture structure in deep crust (Sibson et al., 1986; Chan et al., 2005; Sibson et al., 2017). Sibson (1986) proposed that faults may act as impermeable seals and can transiently become highly permeable pathways for fluid discharge when slip occurs (i.e. earthquake), responsible for episodic mineralization and subsequent vein structure observed. Depending on the source of inflow, faults can behave either as a “pump” or a “valve”. The former involves the coseismic collapse of infilled dilatant fractures, and the latter functions on a fluid reservoir where the rising fluid overpressure induces fault slip and allows partial draining of the reservoir. The fault-valve behavior has been seismically observed in many hydrothermal areas in the upper crust (Miller et al., 2002; Shelly et al., 2015), but remains largely unclear in the lower crust. Here, for the first time, I seismically image such large-scale fault-fluid interaction phenomena in the mid-to-lower crust (11-18 km



depth). The pump-like model is preferred in this case because of the observed radial spreading of aftershocks rather than a linear propagation in most cases in upper crust (Shapiro et al., 2009; Chen et al., 2012). Moreover, the fluid reservoir characterized by high V_p/V_s is above, not below the Meinong fault plane as is required for a fault-valve model. The reservoir is likely formed by the rapidly depositing sediments from the southern Taiwan mountain belt and capped by mudstone-dominated Gutingkeng formation in the area to build up a fluid-rich, overpressurized environment above and around the Meinong mainshock. As shown in Figure 15a, the rupture of the earthquake (white star) then creates new fractures in surrounding porous medium (dilatation in red around the white star) and acts as a pressure source (compressional blue spot indicated by the black arrow) to pump the fluid migration outward (Figure 15b). Crustal permeability has been known as a time-varying property and can be enhanced by seismic waves from distant earthquakes (Elkhoury et al., 2006). In a global compilation study of (Ingebritsen & Mannin, 2010), in the upper crust the seismically-derived permeability is usually two or three orders of magnitude higher than the estimates from the geothermal and laboratory approaches, also suggesting transient increase of permeability. The permeability in the mid-to-lower crust, because of lacking seismic observations, is only derived from petrological models¹ and laboratory experiments (Shmonov et al., 2003), giving values of 10^{-18} to 10^{-19} m² at the depth of ~15 km (Figure

16, blue and black curves). They are considered as long-term values in a geological time scale and far lower than my seismic observations of $3.36 \times 10^{-14} \text{ m}^2$.

More recently, Ingebritsen & Manning (2010) suggested a high and transient permeability-depth curve by compiling high permeability data (Fig. 8, gray curve), which is closer but still one order of magnitude lower than my measurement. The results therefore infer that the permeability can be increased by a factor of ~ 4 during earthquake rupture processes even at the mid-to-lower crustal depths, creating a large-scale fluid flow migration in contrast to microscopic granular fluid flow due to creep cavitation (Fusseis et al., 2009) or nanoscale fluid flow (Plumper et al., 2017). Such coseismic permeability increase is transient but decays slowly in time (Elkhoury et al., 2006; Ingebritsen et al., 2010), and may have more profound influence on the lower crustal fluid circulation. Moreover, if I can only observe fluid-driven aftershocks with the seismogenic permeability (Talwani, 2007), the earthquake-induced fluid flow in mid-to-lower crust may occur more frequently but aseismically. In this case, the mid-to-lower crustal earthquakes could play more important roles than previously thought in modulating fluid circulation and in turn the heat and solute transport in the crust (Manning and Ingebritsen, 1999).

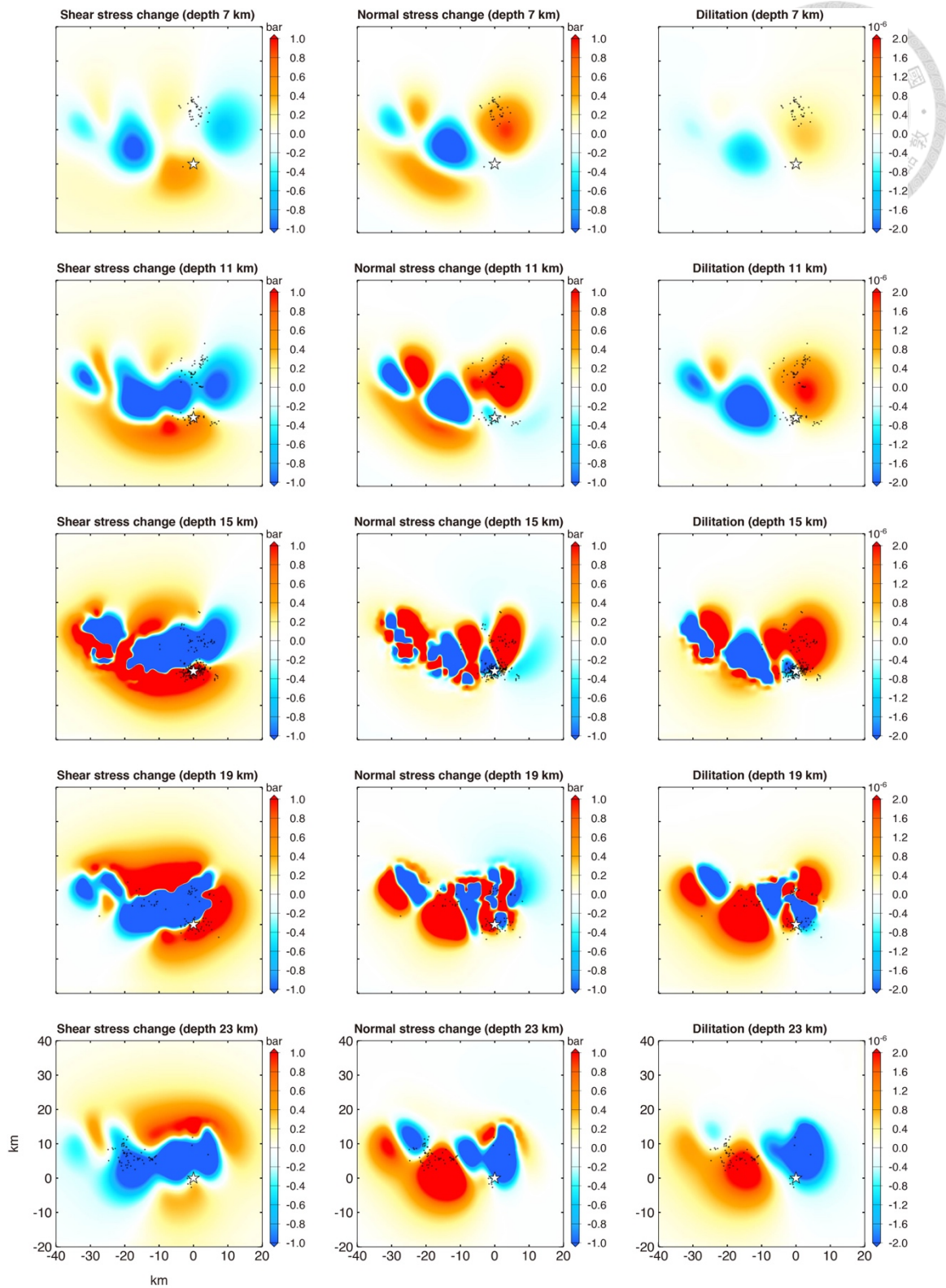


Figure 14 Coseismic Coulomb stress and strain changes of the Meinong earthquake at different depths. The finite fault model is based on Huang et al. (2016). Panels from left to right are the shear stress, normal stress, and dilatational strain changes,

respectively. The red color indicates the stress increase and dilatation; and the blue is vice versa.

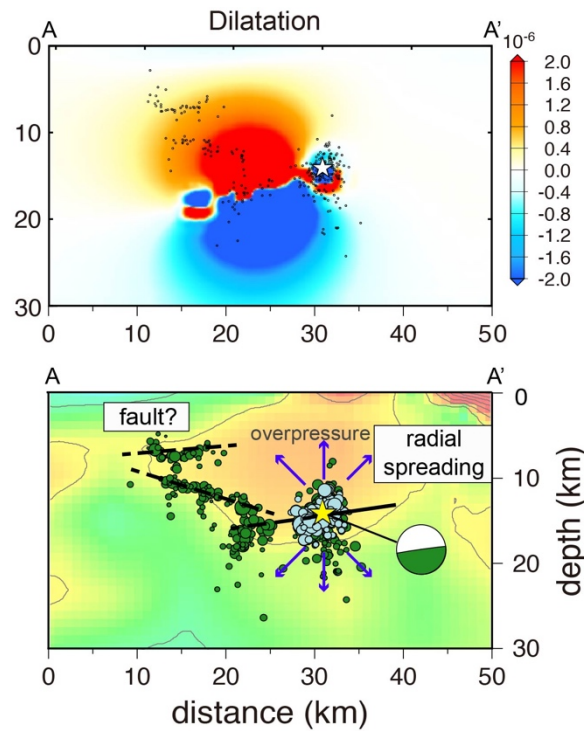


Figure 15 Aftershock distribution with coseismic dilatational strain change (a) and V_p/V_s structure (b) in the cross-section AA' of Fig. 10. The yellow star in **b** denotes the Meinong earthquake that pumps the pore space fluid to migrate radially from the mainshock hypocenter. The blue arrows schematically indicate the fluid flow directions. The black solid and dashed lines denote the seismogenic fault of the Meinong earthquake and the potential triggered faults, respectively.

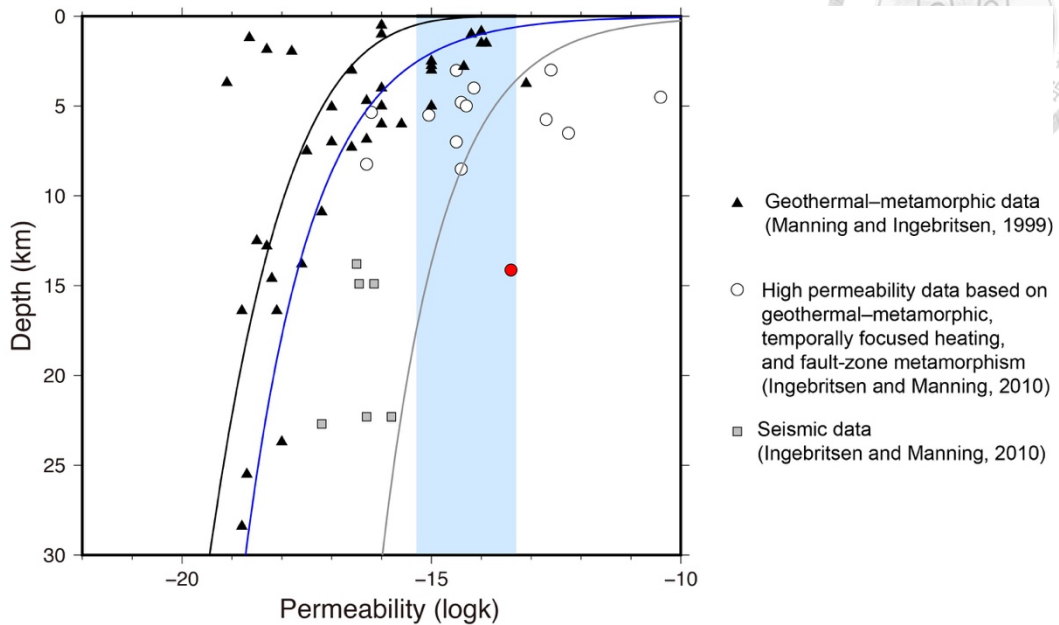


Figure 16 Compiled crustal-scale permeability measurements from seismic and laboratory measurements in previous studies. Black triangles are geothermal-metamorphic data compiled in the work of Manning and Ingebritsen (1999). Gray squares are high permeability data based on geothermal-metamorphic, temporally focused heating, and fault-zone metamorphism data from Ingebritsen and Manning (2010). White dots are seismic data also compiled from Ingebritsen and Manning (2010), and the red dot is my measurement. Note my measurement shows a transient permeability ~ 4 orders greater than the background values at 15 km depth (triangles and squares). The black, blue, and gray curves are regression permeability-depth curves for different datasets (Ingebritsen and Manning, 2010) (see texts for more details). The blue region is the range of semogenic permeability (Talwani et al., 2007).

5.3 Insights from shallow and deep structures



The complicate surface deformation in the Guanmiao-Lungchi area can be attributed to mud diapir of the Lungchan fault (Huang et al., 2016) and pure tectonic movement (Maryline et al., 2017). According to the study of Maryline et al (2017), it infers that the main fault slip of Meinong mainshock triggered (Figure 17) the shallower fault from Huang et al (2016). Then the slip of the shallower fault triggered the Napalin back-thrust and the Houchiali fault, inducing the displacement in the Guanmiao-Lungchi area. However, due to the evidence of overpressure crustal fluid such as high V_p/V_s area, transient high permeability induced by the mainshock and the aftershock migration caused by large-scale fluid flow, the role of overpressure mudstone stratum can't be excluded. Fluid plays an important role controlling the short-term deformation and active tectonic movements in southern Taiwan.

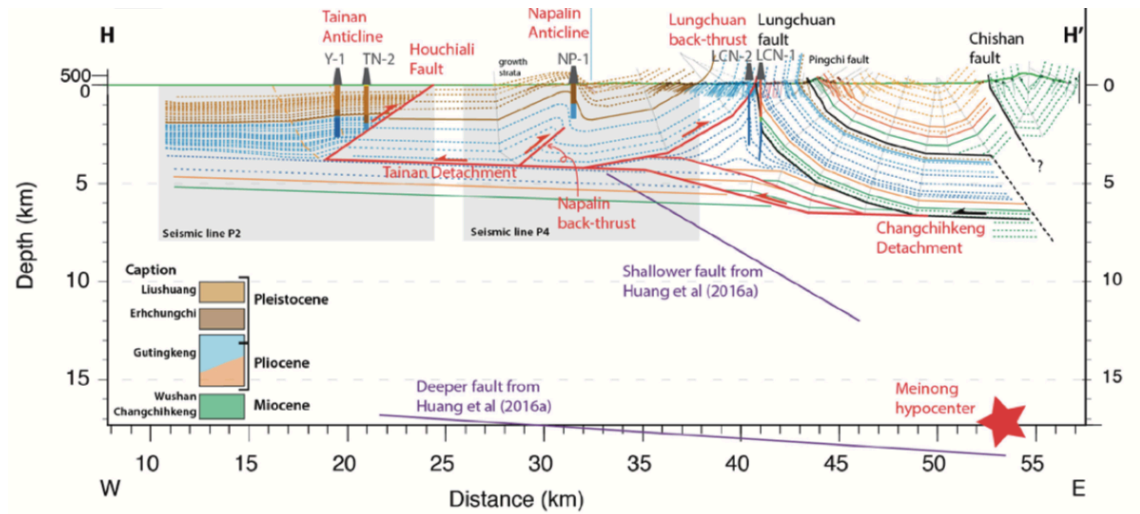
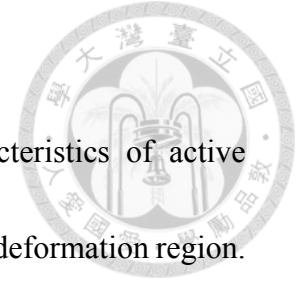


Figure 17 The schematic interpretation from Maryline et al (2017).

Chapter 6 Conclusion



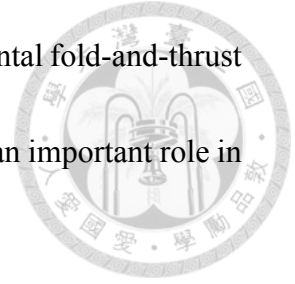
This study uses different techniques to constrain the characteristics of active structures in southwestern Taiwan around the Meinong earthquake deformation region.

The analyses of topography and surface deformation show that two deformational lineaments triggered during the Meinong earthquake fit topographic lineaments, implying multiple seismic events along the two lineaments. The relocation and focal mechanism solutions of aftershocks show that most seismicity occur around a region of high V_p/V_s ratio, implying faulting or fracturing around a mudstone region.

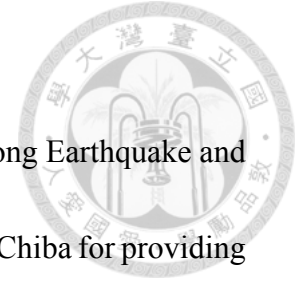
In addition, the spatiotemporal pattern of the aftershock migration around the main shock indicates fluid-driven processes involved. This is the first-time ones can observe fluid-driven seismicity migration at the lower crust. The slip of the mainshock fault may cause the mid-to-lower crustal permeability to be transiently higher than the long-term average by three to four orders of magnitude. Such episodic and large fluctuations of permeability could therefore be important and need to be taken into account when estimating the efficiency of water and carbon cycles from the subducing lithosphere to the Earth's surface.

The mechanisms controlling the active structures at the shallow depths and the deep depths are different and dynamic. The shallow crustal deformation is dominant by active structure. However, the deeper crustal deformation is induced by both tectonic

movements and fluid diffusion. It indicates the complexity of the frontal fold-and-thrust belt of the southwestern Taiwan, and mudstone and fluid may play an important role in deformation and seismic behaviors in southwestern Taiwan.



Acknowledgment

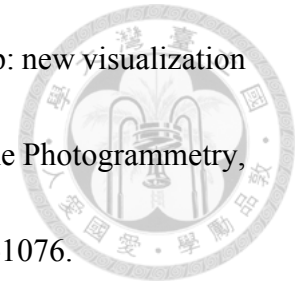


I thank Kyoto University for providing the coseismic data of Meinong Earthquake and National Cheng Kung University for assistant RTK-GPS. I thank T. Chiba for providing tools to produce RRIM on the Internet. I thank Hsin-Hua Huang for providing the methods for aftershock relocation, the velocity model and the instruction and discussion. I thank Mong-Han Huang for providing the mainshock fault of the 2016 Meinong earthquake. Last, I thank Hsin-Hua Huang, Ray Chuang, Kuan-Fu Feng and Mong-Han Huang for helping me to analyze the data and discuss the research together. Thanks to yours, I can finish this research.

Reference

- Chan, Y.-C., Okamoto, K., Yui, T. F., Iizuka, Y., & Chu, H. T. Fossil fluid reservoir beneath a duplex fault structure within the Central Range of Taiwan: implications for fluid leakage and lubrication during earthquake rupturing process. *Terra Nova*, 17, 493-499 (2005).
- Chen, X., Shearer, P. M. & Abercrombie, R. E. Spatial migration of earthquakes within seismic clusters in Southern California: Evidence for fluid diffusion. *J. Geophys. Res.*, 117, B04301, doi:10.1029/2011JB008973 (2012).

Chiba, T., Kaneta, S. I. and Suzuki, Y. (2008), Red relief image map: new visualization method for three dimensional data, *The International Archives of the Photogrammetry, Remote Sensing and Spatial Information Sciences*, 37(B), pp.1071-1076.



Ching, K. E., Rau, R. J., Hu, J. C., and Lee, J. C. (2007), Contemporary deformation of tectonic escape in SW Taiwan from GPS observations, 1995-2005, *Earth and Planetary Science Letters*, 262 (3-4) 601-619.

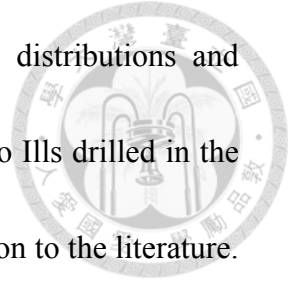
Ching, K.-E., M.-L. Hsieh, K. M. Johnson, K.-H. Chen, R.-J. Rau, and M. Yang (2011), “Modern vertical deformation rates and mountain building in Taiwan from precise leveling and continuous GPS observations”, 2000–2008, *J. Geophys. Res.*, 116, B08406, doi:10.1029/2011JB008242.

Chung, L. H., R. Y. Chuang, J. B. H. Shyu, M. H. Huang, K. M. Yang, K. E. Ching, M. Le Béon, and Y. H. Lee (2016), “Field investigation of shallow structures triggered by the ML6.6 Meinong earthquake, southIstern Taiwan”. *Terr. Atmos. Ocean. Sci.*

Davis, S. D.& Frohlich, C. Single-link cluster analysis of earthquake aftershocks: decay laws and regional variations. *J. Geophys. Res.*, 96, 6336–6350 (1991).

Elkhoury, J. E., Brodsky, E. E. & Agnew D. C. Seismic waves increase permeability. *Nature*, 441, 1,135-8 (2006).

Fusseis, F. *et al.* Creep cavitation can establish a dynamic granular fluid pump in ductile shear zones. *Nature*, 459, doi:10.1038/nature08051 (2009).



Gallegos, T. J. & Varela, B. A. Trends in hydraulic fracturing distributions and treatment fluids, additives, proppants, and water volumes applied to wells drilled in the United States from 1947 through 2010: Data analysis and comparison to the literature.

U.S. Geol. Surv. Sci. Investig. Rep., 2014-5131 (2014).

Goldberg, D. E. Genetic Algorithms in Search, Optimization, and Machine Learning, Addison-Isley, Reading, Massachusetts (1989).

Ho, C. S. (1986). A synthesis of the geologic evolution of Taiwan. *Tectonophysics*, 125(1-3), 1-16.

Hooper, A., Zebker, H., Segall, P., & Kampes, B. (2004). A new method for measuring deformation on volcanoes and other natural terrains using InSAR persistent scatterers. *Geophysical research letters*, 31(23).

Hsieh, M. L., and Knuepfer, P. L. K. (2001) Middle-late Holocene river terraces in the Erhjen River Basin, southern Taiwan-implications of river response to climate change and active tectonic uplift, *Geomorphology*, 38, 337-372.

Huang, C.Y., Yuan, P.B., Lin, C.W. Wang, T.K. and Chang, C.P., (2000). Geodynamic processes of Taiwan arc-continent collision and comparison with analogs in Timor, Papua New Guinea, Urals and Corsica. *Tectonophysics*, 325, 1-21.

Huang, M. H., Hu, J. C., Hsieh, C. S., Ching, K. E., Rau, R. J., Pathier, E., Fruneau, B., and Deffontaines, B. (2006), "A growing structure near the deformation front in SW

Taiwan as deduced from SAR interferometry and geodetic observation”,
GEOPHYSICAL RESEARCH LETTERS, VOL. 33, 1-5. doi:10.1029/2005GL025613.

Huang, M. H., Hu, J. C., Hsieh, C. S., Ching, K. E., Rau, R. J., Pathier, E., Fruneau, B.,
and Deffontaines, B. (2009), “Active deformation of Tainan tableland of southIstern
Taiwan based on geodetic measurements and SAR interferometry”, *Tectonophysics*
466, 322–334.

Huang, H.-H., Wu, Y. M., Lin, T. L., Chao, W. A., Shyu, J. B. H., Chan, C. H., &
Chang, C. H. The Preliminary Study of the 4 March 2010 Mw6.3 Jiasian, Taiwan,
Earthquake Sequence. *Terre. Atmos. Oceanic Sci.*, 22, 3, 283-290 (2011).

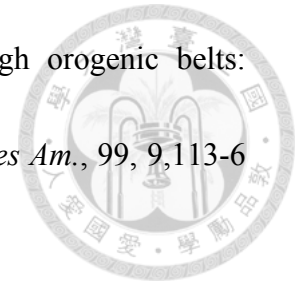
Huang, H.-H., Wu, Y. M., Song, X., Chang, C. H., Lee, S. J., Chang, T. M., & Hsieh,
H. H. Joint Vp and Vs tomography of Taiwan: Implications for subduction-collision
orogeny. *Earth Planet. Sci. Lett.*, 392, 177-191 (2014).

Huang, M.-H., Tung, H., Fielding, E. J., Huang, H. H., Liang, C., Huang, C., & Hu, J.
C. Multiple fault slip triggered above the 2016 Mw 6.4 MeiNong earthquake in Taiwan.
Geophys. Res. Lett., 43, doi:10.1002/2016GL069351 (2016).

Ikari, M. J., Marone, C., Saffer, D. M. & Kopf, A. J. Slip Iakening as a mechanism for
slow Earthquakes. *Nature Geoscience*, 6, DOI: 10.1038/NGEO1818 (2013).

Ingebritsen, S. E. & Manning, C. E. Geological implications of a permeability-depth
curve for the continental crust. *Geology*, 27, 1107–1110 (1999).

Ingebritsen, S. E. & Manning, C. E. Diffuse fluid flux through orogenic belts: implications for the world ocean. *Proc. Natl. Acad. Sci. Unit. States Am.*, 99, 9,113-6 (2002).



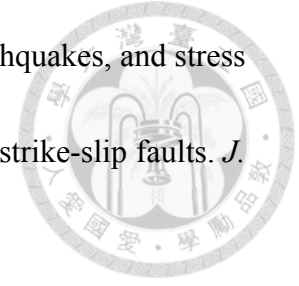
Ingebritsen, S. E. & Manning, C. E. Permeability of the continental crust: Dynamic variations inferred from seismicity and metamorphism. *Geofluids*, 10(1–2), 193–205 (2010).

Kanamori, H., Ye, L., Huang, B. S., Huang, H. H., Lee, S. J., Liang, W. T., ... & Yeh, T. Y. A strong-motion hot spot of the 2016 Meinong, Taiwan, earthquake (Mw=6.4). *Terre. Atmos. Oceanic Sci.*, 28, doi: 10.3319/TAO.2016.10.07.01 (2017).

Keranen, K. M., Savage, H. M., Abers, G. A. & Cochran, E. S. Potentially induced earthquakes in Oklahoma, USA: Links between wastewater injection and the 2011 Mw 5.7 earthquake sequence. *Geology*, G34045.1, doi:10.1130/G34045.1 (2013).

Koketsu, K., & Sekine, S. (1998). Pseudo-bending method for three-dimensional seismic ray tracing in a spherical earth with discontinuities. *Geophysical Journal International*, 132(2), 339-346.

Le-Yang, W. A. N. G., Hua, G. A. O., & Guang-Cai, F. E. N. G. (2017). INSAR AND GPS EARTHQUAKE SOURCE PARAMETER INVERSION FOR THE 2016 Mw6.4 MEINONG, TAIWAN EARTHQUAKE. *Chinese Journal of Geophysics*, 60(4), 346-357.



Lin, J. & Stein, R. S. Stress triggering in thrust and subduction earthquakes, and stress interaction between the southern San Andreas and nearby thrust and strike-slip faults. *J. Geophys. Res.*, 109, B02303, doi:10.1029/2003JB002607 (2004).

Lin, S.-H. A development of double-difference earthquake location program using three-dimensional velocity model and its application to the 2013 Ruisui, Taiwan, earthquake sequence. *National Taiwan University, Master thesis*, 108 pp. (2014).

Liu, C. S., Huang, I. L., & Teng, L. S. (1997). Structural features off southern Taiwan. *Marine Geology*, 137(3-4), 305-319.

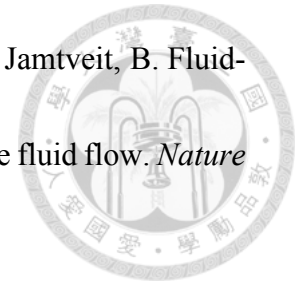
Manga, M., Beresnev, I., Brodsky, E. E., Elkhoury, J. E., Elsworth, D., Ingebritsen, S. E., ... & Wang, C. Y. Changes in permeability caused by transient stresses: Field observations, experiments, and mechanisms, *Rev. Geophys.*, 50, doi:10.1029/2011RG000382 (2012).

Manning, C. E. & Ingebritsen, S. E. Permeability of the continental crust: implications of geothermal data and metamorphic systems. *Rev. Geophys.*, 37, 127-150 (1999).

McGarr, A. Maximum magnitude earthquakes induced by fluid injection. *J. Geophys. Res.*, 119, 1008-1019 (2014).

Peacock, S. M., Christensen, N. I., Bostock, M. G. & Audet P. High pore pressures and porosity at 35 km depth in the Cascadia subduction zone. *Geology*, 39, 5, 471-474 (2011).

Plumper, O., Botan, A., Los, C., Liu, Y., Malthe-Sørenssen, A., & Jamtveit, B. Fluid-driven metamorphism of the continental crust governed by nanoscale fluid flow. *Nature Geoscience*, 10, DOI: 10.1038/NGEO3009 (2017).



Ross, Z. et al. Aftershocks driven by afterslip and fluid pressure slipping through a fault-fracture mesh. *Geophys. Res. Lett.*, 44, doi:10.1002/2017GL074634 (2017).

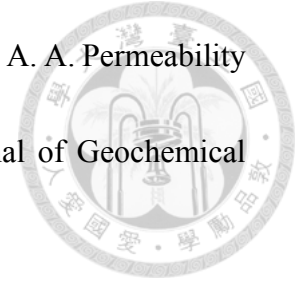
Scuderi, M. M. & Collettini, C. The role of fluid pressure in induced vs. triggered seismicity: insights from rock deformation experiments on carbonates. *Sci. Rep.*, 6, DOI:10.1038/srep24852 (2016).

Secor D. T. Role of fluid pressure in jointing. *Am. J. Sci.*, 263, 633-646 (1965).

Seno T., Stein S., Gripp A.E. A model for the Motion of the Philippine Sea Plate consistent with Nuvel-1 and geological Data. *Geophys. Res.*, 98 (1993), pp. 17941-17948.

Shapiro, S. A., Huenges, E. & Borm, G. Estimating the crust permeability from fluid-injection-induced seismic emission at the KTB site. *Geophys. J. Int.*, 131, F15-F18 (1997).

Shapiro, S. A. & Dinske, C. Fluid-induced seismicity: Pressure diffusion and hydraulic fracturing. *Geophys. Prospect.*, 57, 301-310 (2009).



Shmonov, V. M., Vitiovtova, V. M., Zharikov, A. V. & Grafchikov, A. A. Permeability of the continental crust: implications of experimental data. *Journal of Geochemical Exploration*, 78-79 (2003).

Sibson, R. H. Fluid flow accompanying faulting: Field evidence and models. *Earthquake Prediction, edited by Simpson, D. W. & Richards, P. G., AGU, Washington, D. C*, doi:10.1029/ME004p0593 (1981).

Sibson, R. H. Tensile overpressure compartments on low-angle thrust faults. *Earth, Planets. and Space*, 69, DOI:10.1186/s40623-017-0699-y (2017).

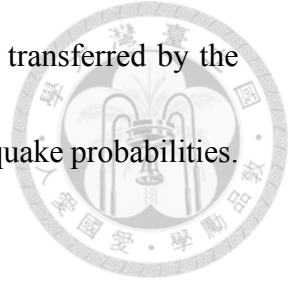
Sun, S. C. (1964). "Photogeologic study of the Tainan-Kaohsiung coastal plain area, Taiwan", *Petrol. Geol. Taiwan*, no. 3, 39-51.

Sun, S.C., Liu, C.S. (1993) Mud diapir and submarine channel deposits in offshore Kaosiung-Hengchun, southIst Taiwan. *Petro Geol Taiwan*, vol.28, p.1-14.

Talwani, P. & Acree, S. Pore pressure diffusion and the mechanism of reservoir-induced seismicity. *Pageoph*, 122, 947-965 (1985).

Talwani P, Chen, L. & Gahalaut, K. Seismogenic permeability, ks. *J. Geophys. Res.*, 112, doi: 10.1029/2006JB004665 (2007).

Tapponnier, P., Peltzer, G., Le Dain, A. Y., Armijo, R., & Cobbold, P. (1982). "Propagating extrusion tectonics in Asia: New insights from simple experiments with plasticine". *Geology*, 10(12), 611-616.



Toda, S., Stein, R. S., Reasenber, P. A. & Dieterich, J. H. Stress transferred by the Mw=6.5 Kobe, Japan, shock: Effect on aftershocks and future earthquake probabilities.

J. Geophys. Res., 103, 24,543-24,565 (1998).

Um, J., & Thurber, C. (1987). A fast algorithm for two-point seismic ray tracing.

Bulletin of the Seismological Society of America, 77(3), 972-986.

Vachon, P. W., Geudtner, D., Mattar, K., Gray, A. L., Brugman, M., & Cumming, I.

(1996). Differential SAR interferometry measurements of Athabasca and Saskatchewan glacier flow rate. *Canadian Journal of Remote Sensing*, 22(3), 287-296.

Wen, S., Yeh, Y. L., Chang, Y. Z., & Chen, C. H. (2017). The seismogenic process of the 2016 Meinong earthquake, southwest Taiwan. *Terrestrial, Atmospheric & Oceanic Sciences*, 28(5).

Wu, Y.-M. & Chaio, L.-Y. Seismic Quiescence before the 1999 Chi-Chi, Taiwan, Mw 7.6 Earthquake. *Bull. Seismol. Soc. Am.*, 96, 321-327 (2006).

Wu, Y. M., Chang, C. H., Zhao, L., Teng, T. L., & Nakamura, M. (2008). A comprehensive relocation of earthquakes in Taiwan from 1991 to 2005. *Bulletin of the Seismological Society of America*, 98(3), 1471-1481.

Wu., Y.-M., Zhao, L., Chang, C.-H. & Hsu, Y.-J. Focal-Mechanism Determination in Taiwan by Genetic Algorithm. *Bull. Seismol. Soc. Am.*, 98, 2, 651-661 (2008).

Ya-Ju Hsua, Shui-Beih Yua, Mark Simonsb, Long-Chen Kuoa, Horng-Yue Chena
(2009), “Interseismic crustal deformation in the Taiwan plate boundary zone revealed
by GPS observations, seismicity, and earthquake focal mechanisms”, Elsevier, Volume
479, Issues 1–2, 4-18.

Yokoyama, R., Shirasawa, M. and Pike, R. J. (2002), Visualizing topography by
openness: a new application of image processing to digital elevation models,
photogrammetric engineering & remote sensing, 68(3), pp.257-265.